Iron deficiency drives metabolic adaptation of red pulp macrophages via ferroportin-SYK signaling and BCAA catabolism to enhance erythrophagocytosis

Pratik Kumar Mandal[1#], Raghunandan Mahadeva[1#], Komal Chouhan[1#], Patryk Slusarczyk[1#], Gabriela Zurawska[1], Marta Niklewicz[1], Matylda Macias[1], Aleksandra Szybińska[1], Aneta Jończy[1], Zhaoyuan Liu[2], Florent Ginhoux[3], Małgorzata Lenartowicz[4], Wojciech Pokrzywa[1], Elizabeta Nemeth[5] and Katarzyna Mleczko-Sanecka[1]

1 International Institute of Molecular and Cell Biology in Warsaw, Poland.

2 Shanghai Institute of Immunology, Department of Immunology and Microbiology, Shanghai Jiao Tong University School of Medicine, Shanghai 200025, China.

3 Shanghai Institute of Immunology, Department of Immunology and Microbiology, Shanghai Jiao Tong University School of Medicine, Shanghai 200025, China; Singapore Immunology Network, Agency for Science, Technology and Research, Singapore 138648, Singapore; Translational Immunology Institute, SingHealth Duke-NUS Academic Medical Centre, Singapore, Singapore.

4 Laboratory of Genetics and Evolution, Institute of Zoology and Biomedical Research, Jagiellonian University, Cracow, Poland.

5 David Geffen School of Medicine at UCLA, Los Angeles, California, United States.

# - equal contribution

To whom correspondence may be addressed: Katarzyna Mleczko-Sanecka, International Institute of Molecular and Cell Biology in Warsaw, 4 Ks. Trojdena Street, 02-109 Warsaw, Poland, E-mail: kmsanecka@iimcb.gov.pl

Abstract

Iron deficiency is the most common nutritional disorder worldwide, yet how individual cell types adjust to iron scarcity remains unclear. Splenic red pulp macrophages (RPMs) are essential for systemic iron homeostasis. They manage exceptionally high iron flux by recycling aged red blood cells through erythrophagocytosis, a specialized form of efferocytosis. However, how RPMs adapt their clearance and metabolic programs to iron deficiency remains unexplored. Here, we show that RPMs from mildly anemic, iron-deficient mice exhibit enhanced erythrophagocytic capacity. Proteomic profiling and flow cytometry revealed expansion and activation of lysosomal and mitochondrial networks, accompanied by elevated mitochondrial respiration. This metabolic rewiring and the increase in erythrophagocytosis depended on branched-chain amino acid (BCAA) catabolism. These responses were distinct from alternative macrophage activation states and absent in liver and peritoneal macrophages. Mechanistically, the low hepcidin-high ferroportin axis and SYK kinase activity emerged as drivers of this functional rewiring. Pharmacological inhibition of SYK or BCAA catabolism blunted iron-deficiency-induced erythrophagocytic and mitochondrial adaptations of RPMs. Together, these findings reveal a non-canonical metabolic reprogramming of RPMs that enhances their specialized clearance functions during systemic iron scarcity, raising possiblity that similar signaling circuits may operate in other efferocytic macrophage subsets under altered ferroportin-SYK axis activity.

Introduction

Efficient clearance of apoptotic cells, termed efferocytosis, is fundamental to tissue homeostasis and the prevention of inflammation by averting the release of potentially damaging intracellular components into the surrounding microenvironment[1–4]. Macrophages, the primary phagocytes responsible for efferocytosis, undergo profound metabolic reprogramming to sustain this process[5]. Lipid metabolite-driven receptor activation (e.g., PPARδ, LXR) promotes continual efferocytosis[6–8] coupled with enhanced glycolysis[9,10], fatty acid oxidation[11], mitochondrial respiration and dynamics[12,13], and an upregulated pentose phosphate pathway[14,15,61]. Among amino acids, the metabolism of arginine [via arginase 1 (ARG1) and ornithine decarboxylase (ODC1)][16], methionine (leading to modulation of DNA methylation)[17], tryptophan [by indoleamine 2,3-dioxygenase 1 (IDO1)][18], and glutamine [via glutaminase-1 (GLS1)-mediated glutaminolysis][19] have well-characterized roles in regulating macrophage function during efferocytosis. However, a critical gap remains in our understanding of how diverse metabolic changes are integrated and regulated across macrophage subsets and specialized efferocytic processes. In particular, very little is known about the metabolic or signaling control of erythrophagocytosis (EP), the process of clearing physiologically aged or damaged red blood cells (RBCs), which is predominantly carried out by red pulp macrophages (RPMs) in the spleen[20–22]. As RBCs constitute the body's largest iron store, their efficient removal and subsequent iron recovery are critical for supporting erythropoiesis[21,22]. Upon engulfment, RBCs are processed within phagolysosomes, releasing heme, which is catabolized by heme oxygenase 1 (HO-1) into ferrous iron (Fe^{2+}) that feeds the cellular labile iron pool (LIP). Within RPMs, iron from the LIP is either stored within ferritin or exported via ferroportin (FPN) to replenish circulating transferrin-bound iron. The iron export capacity of FPN is tightly regulated by hepcidin, a liver-derived hormone that provokes occlusion and/or degradation of FPN, thus ensuring systemic iron homeostasis[23–25]. The central role of RPMs in the maintenance of iron homeostasis is underscored by the functional attenuation in RBC clearance, accompanied by progressive splenic iron accumulation, observed in mice lacking genes essential for RPM development and during physiological aging[26–28]. Emerging evidence indicates that EP is regulated by such factors as pro-inflammatory signals[29–31], the mechanosensitive channel PIEZO1[32] via calcium (Ca^{2+}) signaling[27,32], and iron accumulation[27]. How these or other factors interact to fine-tune EP in response to varying physiological demands, particularly in states of altered iron bioavailability, remains a key unanswered question.

The critical nature of the RPM-driven recycling system takes on new significance in the face of the global burden of iron deficiency, the main cause of anemia, which impacts approximately 1.8 billion people (approximately 30% of the population)[33–36]. According to the 2021 Global Burden of Disease study, anemia ranks as the third leading contributor to years lived with disability worldwide, and, despite its multifactorial origins, dietary iron deficiency remains the primary cause[35,37]. Critically, the prevalence of iron deficiency itself significantly exceeds that of clinically diagnosed anemia and represents a crucial intersection between cellular iron metabolism and public health outcomes, particularly in resource-constrained developing regions[36–38]. Yet, the specific cellular vulnerabilities and the molecular mechanisms orchestrating adaptation to iron deficiency, including those operating within iron-recycling splenic RPMs, remain poorly defined.

Here, we demonstrate that RPMs in iron-deficient (ID) mice exhibit enhanced EP, and we explore how this functional adjustment is regulated by cellular signaling and metabolic rewiring. We reveal that the hepcidin-FPN axis, via regulating Ca^{2+} and spleen tyrosine kinase (SYK) signaling, enhances the EP capacity of RPMs together with their mitochondrial respiration to optimize iron recycling during iron deficiency. Furthermore, we show that RPMs uniquely rely on efficient catabolism of branched-chain amino acids (BCAAs), rich in RBCs, to enhance their EP capacity, and that this metabolic requirement remains under the control of high FPN and SYK. In sum, our findings highlight novel signaling and metabolite-driven mechanisms that shape the functional plasticity of RPMs during limited iron supplies. These insights not only deepen our understanding of RPM biology but may also inform how other macrophage populations adapt to metabolic stress or iron fluctuations in diverse physiological and pathological contexts.

Results

Nutritional iron deficiency increases the EP capacity of RPMs

To investigate the impact of low systemic iron availability on EP and, more broadly, the iron-recycling capacity of RPMs, we employed a murine model of nutritional iron deficiency. To this end, four-week-old female mice were subjected to either an ID diet (<5 ppm iron) or an iron-balanced (IB) control diet (200 ppm iron) for five weeks. Dietary iron restriction resulted in significantly decreased splenic (Figure 1A) and hepatic (Figure 1B) non-heme iron concentrations in the ID group compared to the IB group, confirmed by reduced iron deposition within the splenic red pulp via Perl's staining (Figure S1A). A subtle but significant reduction in cardiac (Figure S1B)

61 non-heme iron was also observed in the ID group, while muscle (Figure S1C) tissue iron content
62 remained unaffected. These data suggested a tissue-specific response to dietary iron restriction,
63 with the spleen and the liver, the organs for iron recycling and storage, being the most affected.
64 Consistent with limited iron delivery, transferrin saturation (Figure 1C) was markedly reduced in
65 ID mice, leading to mild microcytic hypochromic anemia (Figure 1D, S1D, and S1E), which
66 hallmarks iron deficiency. Expectedly, ID mice displayed compensatory mechanisms manifested
67 by splenic stress erythropoiesis, as evidenced by elevated serum erythropoietin (EPO) (Figure S1F)
68 and increased percentage of splenic, but not bone marrow, $CD71^{+}/TER119^{+}$ progenitor cells
69 (Figure 1E and S1G).

70 Next, we aimed to precisely characterize cell-intrinsic iron parameters of RPMs in response to iron-
71 restricted feeding. Consistent with the drop in serum levels of the iron-regulatory hormone hepcidin
72 (Figure 1F), FPN expression in RPMs was significantly elevated in ID mice, as shown by F4/80
73 immunofluorescence in splenic red pulp and by flow cytometric analysis of $F4/80^{high}$ $CD11b^{dim}$
74 RPMs[27] (Figure 1G and 1H). In agreement with boosted iron-export capacity, a marked decrease
75 in total iron content was observed in the magnetically sorted RPMs from ID mice (Figure 1I), along
76 with reduced protein expression of both L- and H-ferritin as assessed by flow cytometry (FTL and
77 FTH1; Figure 1J and 1K), indicating depletion of intracellular iron stores. Furthermore, we detected
78 upregulated levels of transferrin receptor 1 (TFR1) surface expression (Figure 1L), implying a
79 cellular response to iron deficiency. However, paradoxically, despite enhanced iron export, RPMs
80 in ID mice unexpectedly displayed a mild but significant elevation of LIP, as assessed using the
81 Fe^{2+}-specific fluorescent probe FerroOrange (Figure 1M). Consistent with this finding, we also
82 detected mildly elevated reactive oxygen species (ROS) levels in RPMs of ID versus IB mice
83 (Figure 1N).

84 Intrigued by the increased LIP in RPMs of ID mice, we investigated the capacity of EP, the major
85 route for RPM iron acquisition. To this end, following well-established procedures[27,39], we
86 transfused mice with PKH67-labeled RBCs. Strikingly, flow cytometry analysis revealed
87 significantly enhanced phagocytosis of temperature-stressed RBCs (sRBC) by RPMs from ID
88 compared to IB mice, a phenomenon not observed for non-stressed fresh RBCs that were engulfed
89 at comparably negligible levels (Figure 1O). In addition, we evaluated EP capacity across other
90 myeloid populations, including Kupffer cells (KCs) in the liver, macrophages in the bone marrow,
91 and circulating monocytes (Figure 1O). Among these, only KCs showed a statistically significant,

92 albeit modest, increase in EP capacity in iron-restricted mice. Previous work has shown that splenic
93 red pulp sinuses trap aged RBCs, leading to partial hemolysis and subsequent phagocytosis of
94 membrane remnants (RBC ghosts) by RPMs[40]. To distinguish between the clearance of intact
95 sRBCs and RBC ghosts in our model, we intravenously injected mice with sRBCs ubiquitously
96 expressing GFP and stained with PKH26 membrane dye, as described previously[41]. Consistent with
97 our prior results, RPMs from ID mice exhibited increased EP of GFP^+ $PKH26^+$ and GFP-$PKH26^+$
98 sRBCs compared to control IB animals, confirming their enhanced capability for the uptake of both
99 intact RBCs and RBC ghosts (Figure 1P). Likewise, splenic clearance of transfused GFP-positive
100 sRBCs was accelerated in ID mice compared to IB controls (Figure 1Q), further supporting
101 enhanced sRBC removal by RPMs within the low-iron splenic microenvironment. To validate
102 sRBC transfusion assay results, we next assessed intracellular levels of the erythrocyte marker
103 TER119 in RPMs as a measure of endogenous EP capacity[27,42], confirming its elevation in ID mice
104 (Figure 1R). Finally, we verified whether increased EP in low-iron mice is solely driven by
105 macrophage-intrinsic mechanisms or could result from erythrocyte-derived signals. RBC lifespan
106 remained comparable between IB and ID mice (Figure 1S), suggesting that iron restriction did not
107 compromise RBC integrity. Next, exposure of the apoptotic cell marker phosphatidylserine in
108 splenic RBCs was not enhanced in ID compared to IB mice (Figure 1T). Finally, using a co-culture
109 assay of magnetically isolated splenic and circulating RBCs with primary macrophages, we found
110 that while aged splenic RBCs are preferentially sequestered compared to circulating RBCs (Figure
111 1U), iron deficiency does not increase splenic RBC susceptibility to phagocytosis (Figure 1V),
112 implying no induction of RBC "eat-me" signals by iron restriction. Taken together, we uncovered
113 that systemic iron restriction potentiates the cell-intrinsic RBC clearance capacity of RPMs, likely
114 aimed at balancing the increased replenishment of the plasma iron pool by FPN-mediated export.

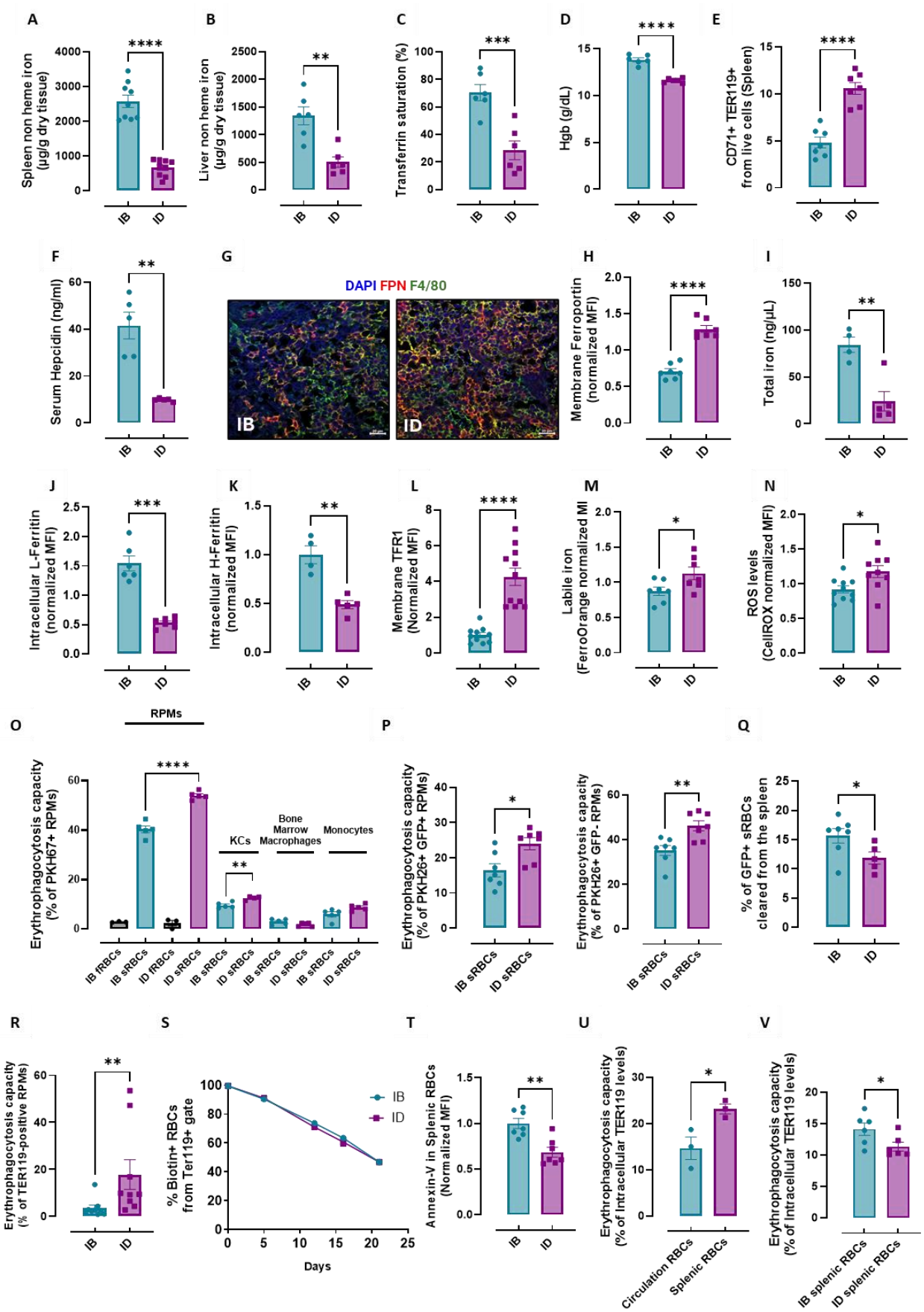
A
Spleen non heme iron (µg/g dry tissue)
B
Liver non heme iron (µg/g dry tissue)
C
Transferrin saturation (%)
D
Hgb (g/dL)
E
CD71+ TER119+ from live cells (Spleen)
F
Serum Hepcidin (ng/ml)
G
DAPI FPN F4/80
IB
ID
H
Membrane Ferroportin (normalized MFI)
I
Total iron (ng/µL)
J
Intracellular L-Ferritin (normalized MFI)
K
Intracellular H-Ferritin (normalized MFI)
L
Membrane TFR1 (Normalized MFI)
M
Labile iron (FerroOrange normalized MI
N
ROS levels (CellROX normalized MFI)
O
RPMs
KCs
Bone Marrow Macrophages
Monocytes
Erythrophagocytosis capacity (% of PKH67+ RPMs)
IB fRBCs
IB sRBCs
ID fRBCs
ID sRBCs
P
Erythrophagocytosis capacity (% of PKH26+ GFP+ RPMs)
Erythrophagocytosis capacity (% of PKH26+ GFP- RPMs)
Q
% of GFP+ sRBCs cleared from the spleen
R
Erythrophagocytosis capacity (% of TER119-positive RPMs)
S
% Biotin+ RBCs from Ter119+ gate
Days
T
Annexin-V in Splenic RBCs (Normalized MFI)
U
Erythrophagocytosis capacity (% of Intracellular TER119 levels)
Circulation RBCs
Splenic RBCs
V
Erythrophagocytosis capacity (% of Intracellular TER119 levels)
IB splenic RBCs
ID splenic RBCs

115

Figure 1. Nutritional iron deficiency increases the erythrophagocytic capacity of RPMs.

(A) Spleen and (B) liver non-heme iron levels, (C) plasma transferrin saturation, and (D) blood hemoglobin (Hgb) were measured in iron-balanced (IB) and iron-deficient (ID) mice. (E) Shown is the percentage of erythroid progenitor cells (TER119^{+} CD71^{+}) present in the spleen of IB and ID mice. (F) Serum hepcidin levels were measured in IB and ID mice with the Hepcidin-Murine Compete ELISA Kit. (G) Representative confocal microscopy images of ferroportin (FPN) protein localization in the splenic red pulp of IB and ID mice. Frozen spleen slices were processed and stained for RPMs (F4/80, green), FPN (red), and nuclei (blue). (H) Expression of FPN on the cell membrane of RPMs derived from IB and ID mice, gated as F4/80^{high}, CD11b^{dim}, was assessed by flow cytometry. (I) The total intracellular iron content in magnetically sorted RPMs from IB and ID mice was assessed using the Iron Assay Kit. (J) Intracellular L-ferritin and (K) H-ferritin protein levels in RPMs of IB and ID mice were quantified by flow cytometry. (L) Expression of TFR1 on the cell membrane of RPMs derived from IB and ID mice was assessed by flow cytometry. (M) Cytosolic ferrous iron (Fe^{2+}) levels in RPMs of IB and ID mice were measured using the FerroOrange probe with flow cytometry. (N) The cytosolic ROS levels in RPMs of IB and ID mice were assessed by determining CellROX Deep Red fluorescence intensity with flow cytometry. (O) The erythrophagocytosis (EP) capacity in RPMs and other myeloid populations of IB and ID mice was determined using flow cytometry by measuring the percentage of cells that phagocytosed transfused PKH67-labeled RBCs. fRBCs indicate fresh RBCs, sRBCs - stressed RBCs (shown only for RPMs; in other indicated populations, fRBCs uptake was negligibly low). (P) IB and ID mice were transfused with GFP-expressing and PKH26-stained sRBCs. The percentage of RPMs positive for intact RBCs (PKH26^{+}GFP^{+}) and RBC ghosts (PKH26^{+}GFP^{-}) was determined. (Q) Flow cytometric analysis of splenic GFP-sRBC percentage in ID vs IB mice. (R) The endogenous EP capacity of RPMs derived from IB and ID mice was determined by intracellular staining of the RBC marker TER119 in RPMs and flow cytometry. (S) The RBC biotinylation lifespan assay was performed on circulating RBCs from IB and ID mice. (T) Flow cytometry assessment of phosphatidylserine exposure (Annexin V staining) in splenic RBCs of ID vs IB mice. (U) EP capacity by primary cultured macrophages (iRPM) was determined using splenic and circulating RBCs of IB mice. (V) EP capacity of iRPMs exposed to RBCs derived from the spleens of IB and ID mice. Each dot represents one mouse or an independent cell-based experiment. Each dot in the graph (S) represents n=9. Data are represented as mean ± SEM. Welch's unpaired t-test determined statistical significance between the two groups. ns $p>0.05$, *$p<0.05$, **$p<0.01$, ***$p<0.001$ and ****$p<0.0001$.

Iron deficiency drives metabolic reprogramming and enhanced lysosomal activity of RPMs via the non-canonical type of polarization

To decipher the molecular mechanisms of enhanced EP capacity in RPMs of ID mice and explore potential accompanying functional changes, we first investigated the transcriptome of FACS-isolated RPMs. Surprisingly, only 145 genes were differentially expressed between RPMs derived from ID and IB mice (Figure 2A, Table S1). Bioinformatic analysis revealed significant enrichment of cell cycle regulators (e.g., *Mki67, Plk1, Plk2, Aurka, E2f7, Sgo1, Kif4, Cenpf, Bub1, Ccnb1, Ccnb2*) among genes upregulated by iron deficiency. This suggested increased pro-mitotic signaling in RPM of ID mice, which was corroborated by elevated protein levels of the proliferation marker Ki67 (Figure 2B). However, this response was not reflected by any significant change in the representation of total RPMs within CD45^{+} splenic cells (Figure 2C). Likewise, using the Ms4a3Cre-RosaTdT reporter mice[43], we found no significant differences in the relative

158 representation of residual embryonically-derived RPMs within the RPM population (Figure 2D),
159 suggesting the absence of their proliferation. The percentage of monocyte-derived RPMs also
160 remained constant at approximately 15% in both IB and ID mice (Figure 2D), implying that the EP
161 enhancement was not driven by *de novo* monocyte recruitment.

162 To further explore the adaptation of RPMs to systemic iron deficiency, we employed TMT-based
163 quantitative proteomics of magnetically-sorted F4/80-high RPMs. This analysis identified 420
164 proteins significantly more abundant and 282 decreased in RPMs of ID mice compared to IB mice
165 (Figure 2E, Table S2). Confirming the quality of the proteomics analysis, we found FTH1 and FTL
166 as the top downregulated hits, and TFR1 as the most induced protein in RPMs of iron-restricted
167 mice. Consistent with this expression pattern, IRP2, a regulator of cellular iron balance, was
168 stabilized in RPMs of ID mice. In agreement with RNA-seq data, we also detected an increase in
169 several regulators of cell cycle progression, such as AURKA, AURKB, PLK1, and CDK1 in RPMs
170 of low-iron mice. Intriguingly, proteomic analysis revealed a pronounced functional rewiring of
171 RPMs in ID mice, highlighting significant post-transcriptional regulation, with far more protein-
172 level alterations and minimal overlap between transcriptomic and proteomic datasets (Figure 2F).
173 First, we observed upregulation of the phosphatidylserine-recognizing phagocytic receptors
174 MERTK and TIM4 (significant hits), and a trend towards induction of AXL and STAB2, along with
175 the Fc receptor CD16 in RPMs of ID mice, responses that were all confirmed by flow cytometry
176 (Figure 2G-H, Figure S2.1A-C). Interestingly, this elevated capacity for recognizing "eat me"
177 signals was accompanied by the induction of the "don't eat me" receptor SIRPα on RPMs in ID
178 mice (Figure S2.1D), hinting at a mechanism that promotes the clearance of aged dysfunctional
179 RBCs, sparing those that are intact. Next, to gain unbiased insights into processes supporting the
180 enhanced EP capacity of RPMs in ID mice, we performed functional enrichment analyses on the
181 differentially expressed proteins. Notably, mitochondrial proteins emerged as the most significantly
182 enriched category among hits upregulated in RPMs of ID compared to IB mice (Figure 2I),
183 including factors involved in ATP synthesis (ATP5S), metabolite transport (SLC25A5, VDAC1),
184 mitochondrial protein import (SAMM50), iron-sulfur cluster assembly (SFXN2), cristae
185 remodeling (MCCC1, PMPCB), and coenzyme Q-10 biosynthesis (COQ9, COQ5). Flow
186 cytometric analysis confirmed these expanded mitochondrial functions by demonstrating a
187 significant increase in both mitochondrial membrane potential (a proxy for mitochondrial activity)
188 (Figure 2J) and mitochondrial mass (Figure 2K) in RPMs of ID mice. Consistently, RPMs of ID

189 *versus* IB mice exhibited increased uptake of fluorescently labeled glucose analog (Figure 2L) and
190 showed a significant upregulation of protein synthesis (Figure 2M), a major ATP-consuming
191 process reflective of enhanced cellular bioenergetics. Interestingly, ATP levels in FACS-sorted
192 RPMs revealed a mild depletion in ID compared to IB mice (Figure 2N), but the activation status
193 of AMPK, a key sensor of cellular energy stress, was not enhanced (Figure 2O). This suggests that
194 RPMs of ID mice did not exhibit energy deficit, but rather a state where increased ATP production
195 is insufficient to meet the high ATP demand driven by accelerated EP and protein synthesis.
196 Importantly, in contrast to RPMs, neither peritoneal macrophages (not involved in iron recycling)
197 nor iron-recycling KCs show hallmarks of metabolic rewiring in ID mice, as exemplified by
198 unaltered mitochondrial activity and mass (Figure S2.1E-H).

199 Further analysis of the proteomic data revealed another major category, encompassing proteins
200 associated with lysosomal functions, as enriched in RPMs of ID compared to IB mice (Figure 2I).
201 In total, RPMs of iron-restricted mice increased the protein levels of 25 key components of the
202 Coordinated Lysosomal Expression and Regulation (CLEAR) network, a transcriptional program
203 that drives lysosomal biogenesis and function[44] (Figure S2.2A). This included integral lysosomal
204 membrane proteins, LAMP1 and LAMP2, vacuolar ATPase subunits (ATP6V0D1, ATP6V0A1),
205 essential for lysosomal acidification, and a diverse array of lysosomal hydrolases, including
206 cathepsins B, D, and S; α-glucosidase (GAA); β-glucosidase (GBA); N-acetylglucosaminidase
207 (NAGA); and sialidase 1 (NEU1). Flow cytometric analysis confirmed elevated intracellular
208 LAMP1 levels (Figure 2P), indicating increased lysosomal mass in RPMs of ID mice. Consistent
209 with this, we observed enhanced lysosomal activity in RPMs of ID mice using a fluorescent probe
210 (Figure 2R). Further ultrastructural analysis of RPMs within splenic sections with TEM revealed
211 that while the number of regular lysosomes, autophagolysosomes, autophagosomes, and
212 peroxisomes remained unaltered between control and low-iron mice, large lysosomes were more
213 abundant in RPMs of iron-restricted mice (Figure S2.2B and S2.2C). While lysosomal size is
214 dynamic and influenced by nutrient availability, emerging evidence, for instance, from senescent
215 cells suggests that a higher proportion of enlarged lysosomes correlates with increased proteolytic
216 activity and lysosomal mass[45,46], remaining consistent with our observations. Taken together, these
217 data suggest that enhanced lysosomal function in RPMs of ID mice is coordinated with heightened
218 RBC clearance, extending the spectrum of RPMs reprogramming in iron deficiency.

219 Erythrocytic heme and iron loading, as well as systemic or cell-intrinsic iron deficiency, have been
220 shown to influence macrophage polarization, promoting either pro-inflammatory or anti-
221 inflammatory profiles, though findings have often been contradictory[47–50]. Since metabolic
222 reprogramming is closely linked to macrophage polarization, which in turn shapes the outcome of
223 infections and inflammatory diseases[51], we assessed the polarization state of RPMs from iron-
224 restricted mice. Our RNA-seq and proteomics data revealed no clear induction of either pro- or
225 anti-inflammatory mediators, alongside a mixed expression pattern of surface signals identified by
226 flow cytometry. While some markers typically associated with M1 (MHCII, CD74) and M2
227 (CD206) polarization were decreased in RPMs of ID *versus* IB mice, others, such as the pro-
228 inflammatory CD38 and the anti-inflammatory CD163, were increased (Figure S2.3). This atypical
229 combination of features suggests that augmented RBC clearance in nutritionally iron-restricted
230 mice leads to the activation state of RPMs distinct from the canonical M1 or M2 type of profile.

231

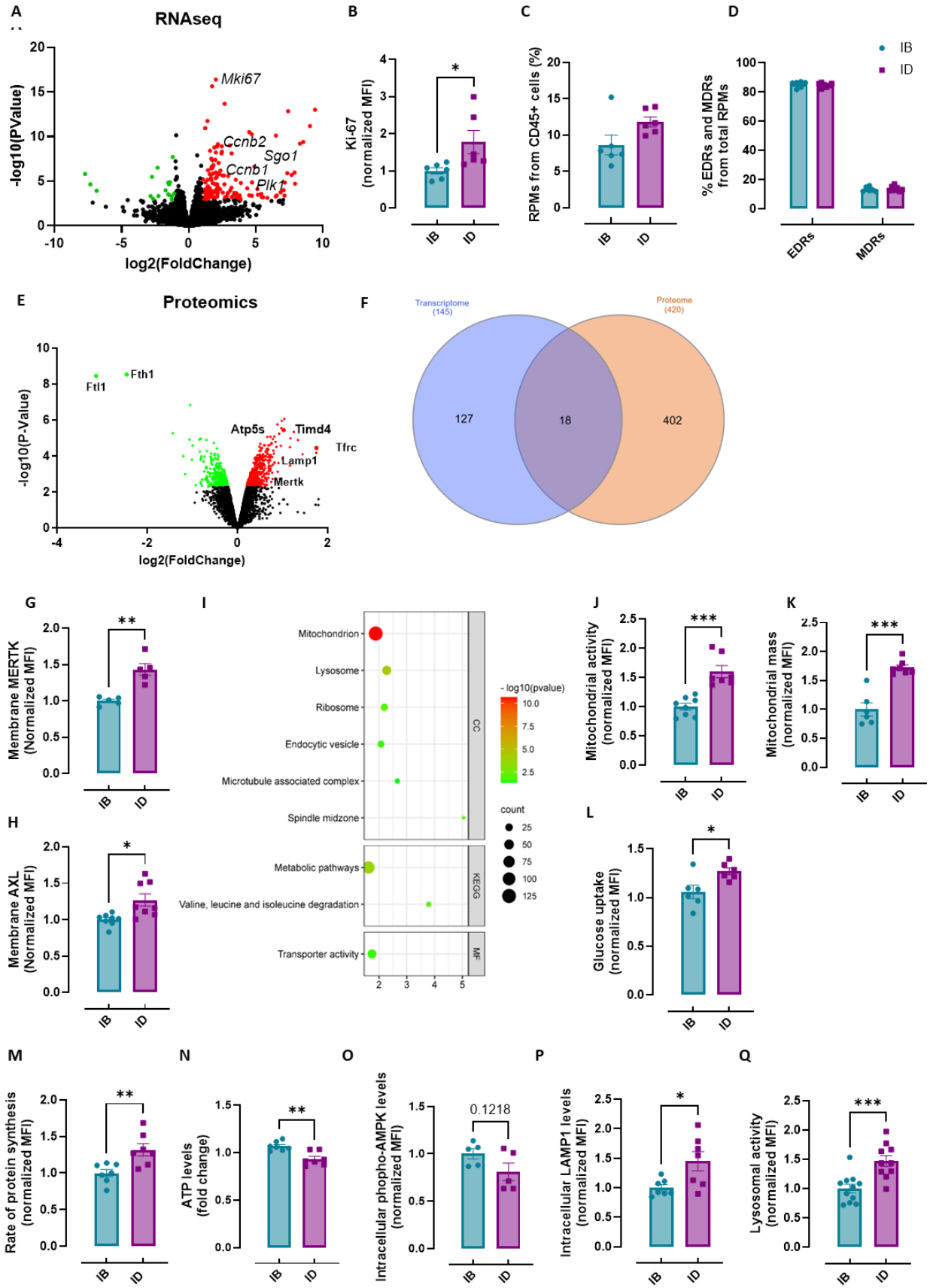
A
RNAseq
-log10(PValue)
log2(FoldChange)
Mki67
Ccnb2
Sgo1
Ccnb1
Plk1
B
Ki-67 (normalized MFI)
IB
ID
C
RPMs from CD45+ cells (%)
D
% EDRs and MDRs from total RPMs
EDRs
MDRs
E
Proteomics
-log10(P-Value)
Fth1
Ftl1
Atp5s
Timd4
Tfrc
Lamp1
Mertk
F
Transcriptome (145)
Proteome (420)
127
18
402
G
Membrane MERTK (Normalized MFI)
H
Membrane AXL (Normalized MFI)
I
Mitochondrion
Lysosome
Ribosome
Endocytic vesicle
Microtubule associated complex
Spindle midzone
Metabolic pathways
Valine, leucine and isoleucine degradation
Transporter activity
CC
KEGG
MF
- log10(pvalue)
count
J
Mitochondrial activity (normalized MFI)
K
Mitochondrial mass (normalized MFI)
L
Glucose uptake (normalized MFI)
M
Rate of protein synthesis (normalized MFI)
N
ATP levels (fold change)
O
Intracellular phopho-AMPK levels (normalized MFI)
0.1218
P
Intracellular LAMP1 levels (normalized MFI)
Q
Lysosomal activity (normalized MFI)

232

233 **Figure 2. Iron deficiency drives metabolic reprogramming and enhanced lysosomal activity of RPMs.**

234 (A) A volcano plot of differentially regulated genes identified by the RNA-Seq transcriptomic analysis in
235 FACS-sorted RPMs derived from IB and ID mice. (B) Intracellular Ki-67 protein levels in RPMs derived
236 from IB and ID mice were assessed by flow cytometry. (C and D) Percentage of (C) total RPMs and (D)
237 embryonic-derived RPMs (EDRs) and monocyte-derived RPMs (MDRs) among total RPMs in IB and ID
238 mice. (E) Volcano plot visualizing the proteomic landscape of RPMs in response to iron deficiency,
239 depicting differentially expressed proteins in IB and ID mice. (F) Venn diagram comparing the differentially
240 expressed genes (transcriptome) and proteins (proteome) in RPMs from ID mice. (G and H) Cell membrane
241 expression levels of (G) MERTK and (H) AXL of RPMs in IB and ID mice were determined by using
242 fluorescently labeled antibodies and flow cytometry. (I) Enriched functional categories among significantly
243 increased protein hits in magnetically sorted RPMs derived from ID versus IB spleen. (J) Mitochondrial
244 membrane potential/activity and (K) mitochondrial mass were determined in RPMs derived from IB and ID
245 mice using TMRE probe and MitoTracker Green, respectively, with flow cytometry. (L) Quantification of
246 glucose uptake via flow cytometry in RPMs from IB and ID mice using a fluorescent glucose analog. (M)
247 Flow cytometric detection of newly synthesized proteins in RPMs of IB and ID mice using Click-iT Plus
248 OPP Alexa Fluor 488 Protein Synthesis Assay. (N) Quantification of ATP levels in FACS-sorted RPMs
249 (10,000 cells) from IB and ID mice using a chemiluminescence-based assay. (O) Intracellular
250 phosphorylated AMPK protein levels in RPMs derived from IB and ID mice were assessed by flow
251 cytometry. (P) Intracellular expression levels of the core lysosomal protein LAMP1 in RPMs of IB and ID
252 mice were determined by flow cytometry. (Q) Flow cytometric assessment of lysosomal activity in RPMs
253 of IB and ID mice using the Lysosomal Intracellular Activity Assay Kit. Each dot represents one mouse.
254 Data are represented as mean ± SEM. Welch's unpaired t-test determined statistical significance between
255 the two groups. ns $p>0.05$, *$p<0.05$, **$p<0.01$, ***$p<0.001$ and ****$p<0.0001$.

256 **Low hepcidin levels are critical for functional adaptations of RPMs during iron deficiency**

257 To elucidate the mechanisms driving the enhanced EP capacity of RPMs in iron deficiency, we first
258 investigated whether these adaptations were directly dependent on intracellular iron levels. Iron
259 depletion *in vitro* using deferiprone (Figure 3A) or DFO[27] did not alter the RBC clearance capacity
260 of primary BMDM macrophages cultured with hemin (iRPM)[27]. Furthermore, our *in vivo* data
261 demonstrated that despite systemic iron deficiency, RPMs in ID mice exhibited elevated LIP
262 (Figure 1M), likely due to their increased EP activity, indicating that iron chelation *in vitro* might
263 not fully recapitulate the complex cellular interactions and signaling pathways present in RPMs *in*
264 *vivo*. These findings suggested that factors beyond simple iron availability may be critical drivers
265 of enhanced RPM phagocytic activity during iron deficiency. To address this possibility
266 mechanistically, we developed an *in vitro* system using iRPMs cultured in serum derived from IB
267 and ID mice, instead of bovine serum. This system recapitulated increased FPN and TFR1
268 expressions in iRPMs exposed to ID serum, without a significant change in total iron levels (Figure
269 3B-D). Notably, cells cultured in ID serum exhibited enhanced EP (Figure S3A), suggesting that
270 serum-borne factor is sufficient to rewire the phagocytic capacity of iRPMs towards RBCs. We
271 first excluded the contribution of EPO, the cytokine previously implicated as a stimulator of
272 efferocytosis[52]. We showed that iRPMs, in contrast to BMDMs cultured without hemin, which is

273 critical to mimic the heme and iron-rich nature of RPMs, did not enhance EP even under high EPO
274 doses (Figure S3B-C). Moreover, PPARγ, a factor proposed to act downstream of EPO[52], failed to
275 alter the EP capacity of iRPMs (Figure S3C). Next, inspired by a study that revealed low hepcidin,
276 rather than iron deficiency itself, as a key driver of pro-inflammatory responses in iron-restricted
277 mice[50], we hypothesized that reduced serum hepcidin levels and enhanced FPN stabilization in
278 RPMs might play a critical role in the adaptive reprogramming of these cells. Strikingly, a 4-h
279 treatment with the hepcidin mimetic PR73 reversed the enhanced EP phenotype in iRPMs exposed
280 to ID, but not to IB serum (Figure 3E and S3D). Likewise, we conducted live imaging of EP by
281 cultured iRPMs incubated with serum from IB and ID mice, and exposed to sRBCs labeled with a
282 dedicated pHrodo™ dye that remains non-fluorescent at neutral pH but emits fluorescence in acidic
283 environments, indicating sequestrations in phagolysosomes. In line with our flow cytometry
284 results, we observed enhanced pHrodo signal in real time in iRPMs treated with ID serum,
285 reflecting their enhanced EP capacity (Figure 3F). This boost of RBC clearance capacity was
286 significantly abrogated upon 4 h of PR73 treatment (Figure 3F). Consistent with our *in vivo*
287 observations, ID serum induced a significant increase in both mitochondrial and lysosomal activity,
288 which was likewise abrogated by PR73 treatment (Figure S3E-H).

289 To follow these *in vitro* observations, we next administered IB and ID mice with PR73 via
290 intraperitoneal injection 4 h before analysis. PR73 administration effectively reduced cell-surface
291 FPN expression and induced hypoferremia in both dietary groups (Figure 3G-H). However, total
292 RPM iron content remained unchanged in both IB and ID mice following PR73 treatment (Figure
293 3I). PR73 administration did not reverse the increased cell surface expression of TFR1 on RPMs
294 of ID mice but instead led to its further elevation, in contrast to IB mice, where TFR1 levels
295 remained unaltered (Figure 3J). Interestingly, PR73 elicited similarly distinct effects on the LIP in
296 RPMs depending on the dietary regimen: it expectedly increased LIP levels in IB mice, but led to
297 a mild decrease in ID mice (Figure 3K). The latter pattern was, strikingly, closely reflected by the
298 pronounced reversal of the elevated EP capacity of RPMs from ID mice by PR73 injection (Figure
299 3L). Likewise, PR73 abrogated most of the other hallmarks of RPM adaptation to iron deficiency,
300 including elevated mitochondrial activity, increased glucose uptake, and heightened protein
301 synthesis (Figure 3M-O). Intriguingly, these modulating effects of PR73 were absent in IB mice.
302 Furthermore, *ex vivo* freshly isolated RPMs exhibited substantially elevated oxidative
303 phosphorylation (OXPHOS), as assessed by oxygen consumption rate measurement with Seahorse

304 (Figure 3P). Strikingly, a 4-h preincubation of the *ex vivo* RPMs of ID mice with PR73 completely
305 abolished their activated oxygen consumption (Figure 3P). Of note, these rapid effects of PR73 did
306 not include changes in the mitochondrial mass of RPMs, remaining elevated regardless of PR73
307 injection in ID mice (Figure S3I). Similarly, lysosomal activity of RPMs of ID mice remained
308 higher than in IB mice despite PR73 supplementation, suggesting either distinct regulatory
309 mechanisms or differential kinetics governing these responses (Figure S3J). To support the key role
310 of the hepcidin-FPN axis in modulating the iron-recycling activity of RPMs, we employed *Tmprss6*
311 knockout (KO) mice, a model of iron-refractory iron deficiency anemia (IRIDA)[53–55]. This model
312 exhibits some characteristics of the nutritional ID model, including reduced transferrin saturation,
313 decreased hepatic iron stores (Figure S3K-L), and anemia. However, in contrast to dietary ID
314 conditions, *Tmprss6* KO mice display elevated hepcidin levels, and their splenic iron stores remain
315 largely unchanged[56,57], with no significant depletion observed, consistent with our findings (Figure
316 S3M). Importantly, we observed no significant difference in RPMs' EP capacity between *Tmprss6*
317 KO mice and wild-type controls (Figure 3Q). Likewise, *in vitro* cultured iRPMs showed no
318 difference in RBC clearance when exposed to serum from either *Tmprss6* KO or wild-type mice
319 (Figure 3R). In sum, these data implied that deficient hepcidin levels and FPN stabilization,
320 hallmarks of nutritional ID, are key driving factors for enhanced RPM erythrophagocytic capacity
321 and their metabolic adaptation to low systemic iron levels.

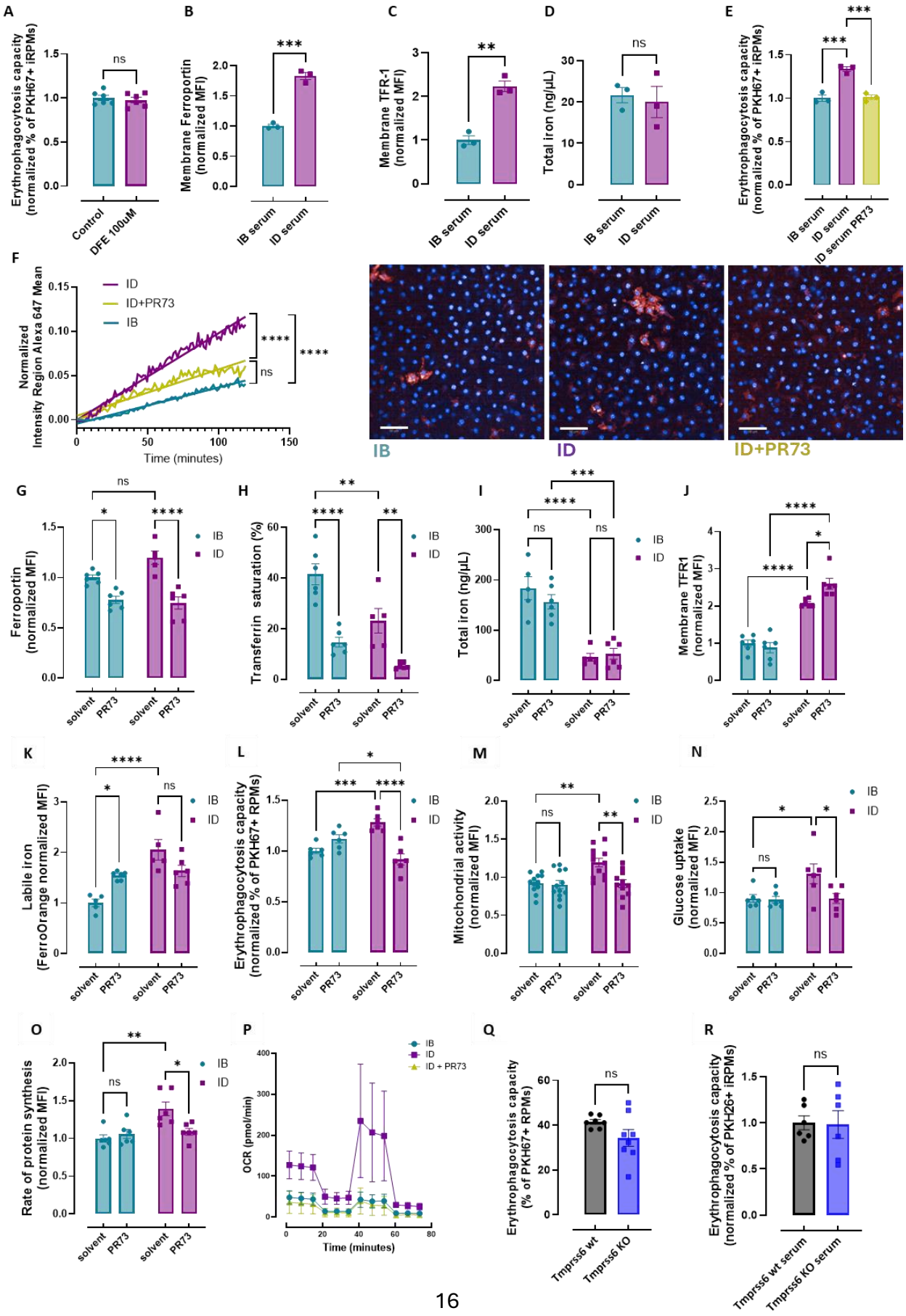
A
Erythrophagocytosis capacity (normalized % of PKH67+ iRPMs)
ns
Control
DFE 100uM
B
Membrane Ferroportin (normalized MFI)
***
IB serum
ID serum
C
Membrane TFR-1 (normalized MFI)
**
IB serum
ID serum
D
Total iron (ng/µL)
ns
IB serum
ID serum
E
Erythrophagocytosis capacity (normalized % of PKH67+ iRPMs)
***
***
IB serum
ID serum
ID serum PR73
F
Normalized Intensity Region Alexa 647 Mean
ID
ID+PR73
IB
****
****
ns
Time (minutes)
IB
ID
ID+PR73
G
Ferroportin (normalized MFI)
ns
*
****
IB
ID
solvent
PR73
H
Transferrin saturation (%)
**
****
**
I
Total iron (ng/µL)
***
****
ns
ns
J
Membrane TFR1 (normalized MFI)
****
****
*
K
Labile iron (FerroOrange normalized MFI)
****
*
ns
L
Erythrophagocytosis capacity (normalized % of PKH67+ RPMs)
*
***
****
M
Mitochondrial activity (normalized MFI)
**
ns
**
N
Glucose uptake (normalized MFI)
*
*
ns
O
Rate of protein synthesis (normalized MFI)
**
ns
*
P
OCR (pmol/min)
IB
ID
ID + PR73
Time (minutes)
Q
Erythrophagocytosis capacity (% of PKH67+ RPMs)
ns
Tmprss6 wt
Tmprss6 KO
R
Erythrophagocytosis capacity (normalized % of PKH26+ iRPMs)
ns
Tmprss6 wt serum
Tmprss6 KO serum

322

Figure 3. Low hepcidin levels are critical for functional adaptations of RPMs during iron deficiency. (A) Normalized EP capacity of PKH67-stained sRBCs by cultured iRPMs treated with an iron chelator DFE (100 μM, 18 h). (B-C) Flow cytometry analysis of (B) surface FPN and (C) TFR1 expression on iRPMs cultured with serum from IB or ID mice. (D) The total intracellular iron content in iRPMs cultured with serum from IB or ID mice was assessed using the Iron Assay Kit. (E) The EP capacity in iRPMs cultured with serum from IB or ID mice, and serum from ID mice supplemented with the hepcidin agonist PR73 (2 μg/mL, 4 h) determined using flow cytometry by measuring the percentage of cells that phagocytosed PKH67-labeled RBCs. (F) Time-lapse imaging of the EP progression in iRPMs, exposed to pHrodo-stained sRBCs and cultured with the serum from IB and ID mice (with and without 4 h pretreatment with PR73). The left panel shows the quantification of the RBC fluorescent signal over time, normalized to the number of macrophages. The right panel shows example images at the endpoint of the assay. Scale bar=50 μm. (G) Flow cytometric analysis of FPN cell surface expression on RPMs from IB and ID mice following intraperitoneal administration of the hepcidin agonist PR73 (50 nmol/mouse, 4 h). (H) Plasma transferrin saturation was determined in IB and ID mice following PR73 administration. (I) Intracellular iron content in magnetically sorted RPMs from IB and ID mice post-PR73 treatment as determined using the Iron Assay Kit. (J) Flow cytometric evaluation of TFR1 surface expression on RPMs derived from IB and ID mice post-PR73 administration. (K) Flow cytometric measurement of cytosolic ferrous iron (Fe^{2+}) levels in RPMs from IB and ID mice using FerroOrange following PR73 administration. (L) Normalized EP capacity of PKH67-sRBCs by RPMs from IB and ID mice after PR73 administration. (M) Mitochondrial activity was determined in RPMs derived from IB and ID mice using the TMRE probe post-PR73 administration, with flow cytometry. (N) Quantification of glucose uptake via flow cytometry in RPMs from IB and ID mice upon PR73 administration using a fluorescent glucose analog. (O) Flow cytometric detection of newly synthesized proteins in RPMs of IB and ID mice using Click-iT Plus OPP Alexa Fluor 488 Protein Synthesis Assay after PR73 administration. (P) Seahorse analysis of *ex vivo* RPMs from IB and ID mice, with or without 4 h PR73 preincubation for RPMs from ID mice. (Q) Flow cytometric assessment of EP capacity in RPMs of *Tmprss6* wt and *Tmprss6* KO mice was quantified as the percentage of cells engulfing PKH67-labeled sRBCs. (R) Normalized EP capacity of PKH26 sRBCs by cultured iRPMs treated with serum from *Tmprss6* wt and *Tmprss6* KO mice was determined using flow cytometry. Each dot represents one mouse or an independent cell-based experiment. Data are represented as mean ± SEM. Welch's unpaired t-test determined statistical significance in A-D and Q-R, while two-way ANOVA with Tukey's Multiple Comparison tests was used in G-O. A one-way ANOVA test with Dunnett's or Tukey's Multiple Comparison tests was used in E. In F, the significant differences between the slopes of simple linear regression lines are shown. ns $p>0.05$, *$p<0.05$, **$p<0.01$, ***$p<0.001$ and ****$p<0.0001$.

Elevated FPN regulates RPM rewiring in ID conditions via Ca^2-dependent signaling

To further assess the role of FPN upregulation in RPM rewiring under systemic ID conditions, we used lentiviral transduction to create iRPMs with enforced FPN overexpression (FPN OE; FPN-iRPMs) and assessed whether this mimics RPM adaptation to iron deficiency. Control iRPMs were generated using an empty vector without the *Slc40a1* gene, encoding FPN (mock-iRPMs). We confirmed significant FPN elevation on the surface of FPN-iRPMs compared to control cells (Figure 4A). This further led to the elevation of TFR1 surface expression but did not significantly change the total iron levels (Figure 4B-C), thus resembling the iRPMs exposed to ID vs IB serum. Under basal conditions, we quantified the LIP in both FPN-iRPMs and mock-iRPMs, finding no significant difference (Figure 4D). In an attempt to recapitulate the mildly elevated LIP observed in RPMs of ID mice during enhanced *in vivo* EP, we next sought to mimic the splenic

367 microenvironment by continuously exposing iRPMs to sRBCs during culture. Strikingly, sRBC-
368 exposed FPN-iRPMs exhibited a significant increase in LIP compared to mock-iRPMs (Figure
369 4D), mirroring the *in vivo* RPM response (Figure 1M). Most importantly, FPN-iRPMs displayed
370 enhanced RBC clearance regardless of sRBC exposure during culture (Figure 4E), a response that
371 was efficiently reversed by suppression of FPN by a potent specific inhibitor vamifeport[58] (Figure
372 4F). These findings demonstrate that forced FPN expression and consequent increased cellular iron
373 flux, rather than overall iron content, specifically stimulate EP.

374 We next investigated in more detail the potential metabolic consequences of increased FPN
375 expression. FPN overexpression led to a significant increase in both mitochondrial activity and
376 mass compared to mock-transduced iRPMs in a manner that was likewise blocked by vamifeport
377 (Figure 4G-H). This response was reflected by a vamifeport-controlled increase in glucose uptake
378 and protein synthesis rate in FPN-overexpressing iRPMs (Figure 4I-J), suggesting a coordinated
379 metabolic adaptation. Importantly, these responses were independent of the presence of sRBCs in
380 the culture media and intracellular iRPM LIP levels (Figure S4A-D), indicating a regulatory effect
381 of FPN on mitochondrial functions that may reach beyond its role as a regulator of intracellular
382 iron status.

383 We next set out to elucidate the signaling mechanisms underlying the functional rewiring of RPMs
384 in response to increased FPN expression during systemic iron deficiency. Our previous work
385 demonstrated that age-related iron overload, likely due to low FPN expression, suppressed RPM's
386 RBC clearance capacity[27]. This phenomenon was recapitulated in iron-loaded *in vitro* iRPMs and
387 was reflected by reduced intracellular Ca^{2+} levels[27], a key regulatory signal for macrophage
388 phagocytosis[32,59]. Extending this observation, we found a significant increase in intracellular Ca^{2+}
389 levels within RPMs of ID mice compared to IB mice (Figure 4K), mirroring the enhanced RBC
390 clearance capacity. Notably, PR73 administration reversed the elevated intracellular Ca^{2+} levels
391 specifically in RPMs of ID mice, with no effect observed in RPMs of IB mice (Figure 4L). In
392 parallel, iRPMs exposed to ID serum also displayed increased Ca^{2+} levels, a response likewise
393 suppressed by PR73 treatment (Figure 4M). This demonstrates that intracellular Ca^{2+} signaling,
394 like phagocytic and mitochondrial activities, is uniquely reprogrammed in RPMs of iron-deficient
395 mice in a manner dependent on low hepcidin/high FPN. Consistently, FPN-iRPMs exhibited
396 increased intracellular Ca^{2+} levels compared to mock-iRPMs, independent of the presence of
397 stressed RBCs during culture and cellular LIP levels, further implying the role of Ca^{2+} signaling in

398 RPM functional rewiring driven by high FPN (Figure 4N). To further examine whether enhanced
399 Ca^{2+} signaling may support increased EP in iRPMs, we employed both intracellular (BAPTA-AM)
400 and/or extracellular (EGTA) Ca^{2+} chelators in the FPN-iRPM model and iRPMs exposed to ID and
401 IB serum (Figure 4O-P). Both chelation strategies not only reduced the overall EP capacity of
402 iRPMs but also effectively suppressed the enhancement of RBC clearance in FPN-high conditions.
403 Recent findings implied that FPN may have the capacity for Ca^{2+} import[60]. To test whether FPN-
404 mediated Ca^{2+} influx directly drives their functional rewiring, we employed overexpression of the
405 FPN variant harboring a specific aspartate-to-alanine mutation (D39A), expected to disrupt the
406 unidirectional movement of Ca^{2+} into the cell while preserving Fe^{2+} transport function[54].
407 Interestingly, we found no significant differences in the enhancement of EP or intracellular Ca^{2+}
408 levels between iRPMs overexpressing mutant D39A and wild-type FPN (Figure 4Q-R). In sum,
409 our findings suggested that FPN-mediated activation of Ca^{2+} signaling, likely through an indirect
410 mechanism, contributes to enhanced phagocytic capacity of RPMs.

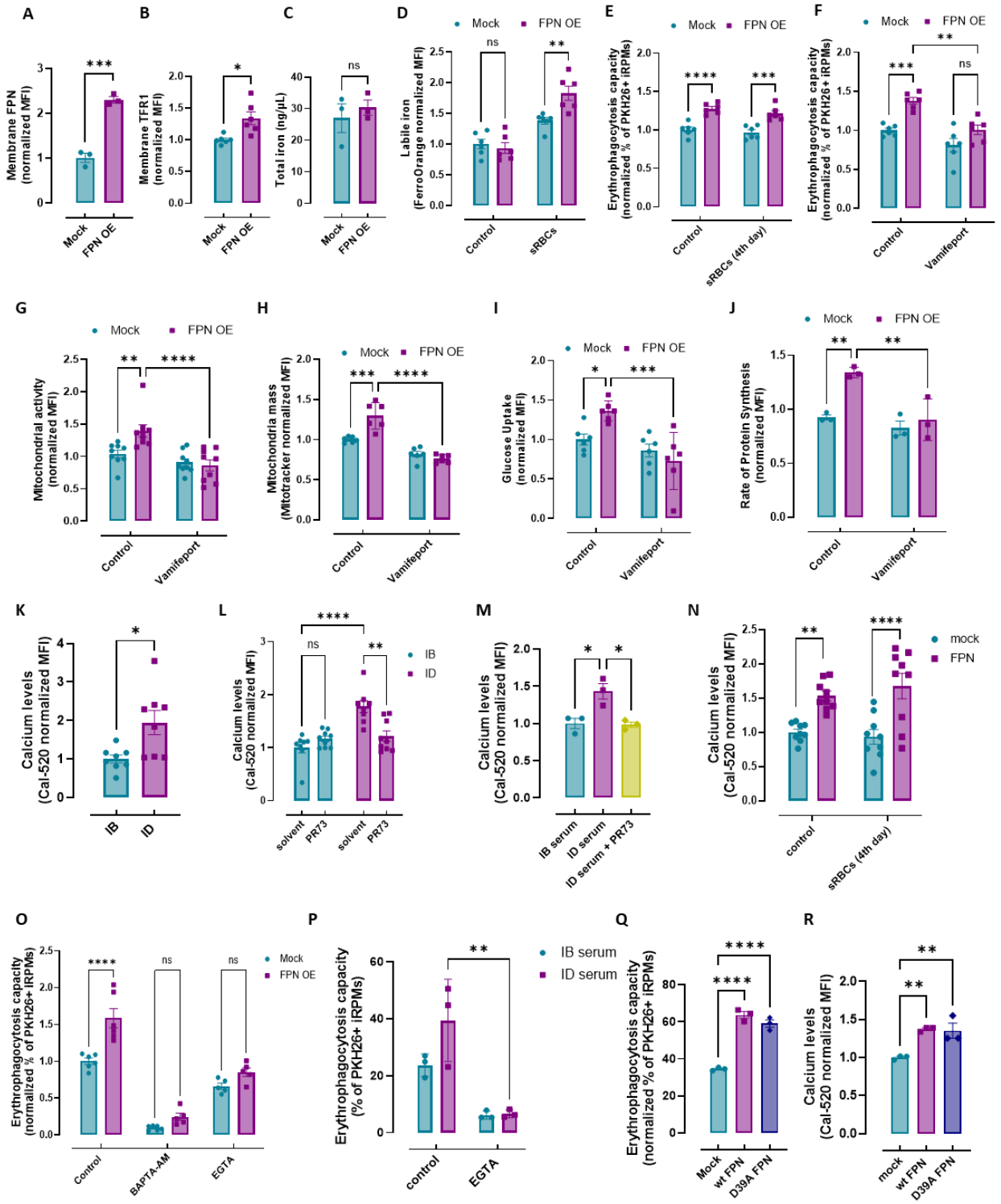

Figure 4. Elevated FPN regulates RPM rewiring in ID conditions via Ca²-dependent signaling.

(A-J) Lentiviral transduction was used to generate iRPMs overexpressing FPN (FPN OE; FPN-iRPMs) or expressing an empty vector (mock). (A-C) Flow cytometric analysis of (A) FPN and (B) TFR1 cell surface expression, and (C) intracellular iron content in mock and FPN-iRPMs determined using the Iron Assay Kit. (D) Flow cytometric measurement of cytosolic ferrous iron (Fe^{2+}) levels in mock and FPN-iRPMs with and

without sRBC exposure during culture. (E) Normalized EP capacity towards PKH26-sRBCs by mock and FPN-iRPMs with and without sRBC exposure during culture was determined with flow cytometry. (F-J) iRPMs were cultured with sRBCs and treated with vamifeport (20 µM, 15 h). (F) Normalized EP capacity towards PKH26-sRBCs was determined by flow cytometry. (G) Mitochondrial activity and (H) mass were determined by the TMRE and MitoTracker Green probes, respectively, and flow cytometry. (I) Quantification of glucose uptake via flow cytometry using a fluorescent glucose analog. (J) Flow cytometric detection of newly synthesized proteins using Click-iT Plus OPP Alexa Fluor 488 Protein Synthesis Assay and flow cytometry. (K) Cytosolic calcium iron (Ca^{2+}) levels in RPMs of IB and ID mice were measured using Cal-520 fluorescent probe with flow cytometry. (L) Cytosolic Ca^{2+} levels in RPMs of IB and ID mice were measured with flow cytometry post-PR73 administration using Cal-520 fluorescent probe with flow cytometry. (M) Cytosolic Ca^{2+} levels in iRPMs cultured with serum from IB or ID mice and serum from ID mice treated with the hepcidin agonist PR73 (2 µg/mL, 4 h) were determined using Cal-520 fluorescent probe with flow cytometry. (N) Flow cytometric measurement of cytosolic Ca^{2+} levels in mock and FPN-iRPMs with and without sRBC exposure using Cal-520 fluorescent probe with flow cytometry. (O) Normalized EP capacity of PKH26-sRBCs by mock and FPN-iRPMs treated with an intracellular (BAPTA-AM; 10 µM, 1 h) and extracellular (EGTA; 3 mM, 30 min) calcium chelator. (P) The EP capacity in iRPMs cultured with serum from IB and ID mice, and treated with extracellular (EGTA; 3 mM, 30 min) calcium chelator, was determined using flow cytometry by measuring the percentage of cells that phagocytosed PKH26-labeled sRBCs. (Q) Flow cytometric assessment of EP capacity in mock-transduced iRPMs and iRPMs overexpressing wild-type FPN and FPN mutant D39A was quantified as the percentage of cells engulfing PKH26-labeled RBCs. (R) Flow cytometric measurement of cytosolic Ca^{2+} levels in mock, FPN, and D39A-iRPMs using Cal-520 fluorescent probe with flow cytometry. Each dot represents one mouse or an independent cell-based experiment. Data are represented as mean ± SEM. Welch's unpaired t-test determined statistical significance in A-C and K. Two-way ANOVA with Tukey's Multiple Comparison tests was used in D-J, N, and N-P. A one-way ANOVA test with Dunnett's or Tukey's Multiple Comparison tests was used in M and Q-R. ns $p>0.05$, *$p<0.05$, **$p<0.01$, ***$p<0.001$ and ****$p<0.0001$.

SYK kinase mediates the FPN-dependent adaptation of RPMs to ID conditions

Expanding on prior knowledge, we next sought to identify the genetic mediators of Ca^{2+}-dependent signaling underlying the functional rewiring of RPMs in ID mice. First, we examined the involvement of PIEZO1, a mechanoreceptor identified to modulate Ca^{2+} signaling and EP in RPMs[32]. Indeed, under basal conditions, treatment of iRPMs *in vitro* with the PIEZO1 activator YODA1 and the inhibitor GsMTx1 mildly affected EP (Figure S5.1A-B). However, GsMTx1 did not significantly affect the enhanced EP capacity observed in iRPMs exposed to ID serum (Figure S5.1C). These findings excluded a major role for PIEZO1 in mediating the functional acceleration of RPMs in response to iron deficiency.

To further dissect the Ca^{2+}-dependent signaling pathways responsible for the enhanced EP observed in RPMs during iron deficiency, we performed a targeted pharmacological screen. Inhibitors of CaMKK (STO-609), calmodulin-mediated signaling (W7), P2 receptor-mediated Ca^{2+} signaling (Apyrase)[59], and macropinocytosis (EIPA) had no discernible impact on EP in either mock or FPN-iRPMs (Figure 5A). Likewise, despite its well-established role in Ca^{2+}-dependent signaling, inhibition of protein kinase C (PKC) with Bisindolylmaleimide I did not reduce EP in either mock-

458 or FPN-iRPMs (Figure 5A). However, the inhibition of the spleen tyrosine kinase (SYK), a
459 downstream effector of PKC-dependent signaling, with piceatannol completely abolished the
460 increased EP in FPN-iRPMs *versus* mock-transduced iRPMs (Figure 5A). To mitigate the potential
461 off-target effects of piceatannol, we next employed the highly selective SYK inhibitor entospletinib
462 (ENTO; also known as GS-9973) in mock- and FPN-iRPM cultures. Consistently, ENTO
463 effectively suppressed FPN-driven EP enhancement in FPN-iRPMs and iRPMs cultured in ID
464 versus IB serum (Figure 5B-C). Furthermore, we observed that ENTO prevented an increase in
465 Ca^{2+} levels upon FPN overexpression (Figure 5D). Interestingly, supplementation with ENTO was
466 sufficient to reduce both the mitochondrial activity and mass of iRPMs overexpressing FPN to the
467 control levels of mock-transduced cells (Figure 5E-F).

468 Next, we sought to investigate the role of SYK in RPM iron recycling *in vivo.* First, we found that
469 a 4 h treatment of ID mice with PR73 markedly reduced levels of the active form of SYK, phospho-
470 SYK (Y525/526), in RPMs, whereas no significant effect of the hepcidin agonist was observed in
471 RPMs from IB mice (Figure 5G), similarly to all previous ID-specific suppressive effects of PR73
472 on RPM rewiring phenotypes. We further assessed the impact of the SYK inhibition with ENTO in
473 both IB and ID mice. Oral daily ENTO administration for the last 2 weeks of the iron-modified
474 diet (5 mg/kg/day; with flavored jellies) effectively reduced phospho-SYK (Y525/526) levels in
475 RPMs from both IB and ID mice compared to vehicle controls (Figure 5H). Strikingly, ENTO
476 administration led to a marked reduction in the EP capacity of RPMs, specifically in ID mice, while
477 EP in IB mice remained unaffected by ENTO treatment (Figure 5I). Furthermore, ENTO treatment
478 partially reversed the increase in Ca^{2+} levels in RPMs observed between ID and IB mice (Figure
479 5J). Interestingly, ENTO also suppressed FPN induction associated with iron deficiency (Figure
480 5K), suggesting that EP capacity and FPN expression may be bidirectionally linked. The
481 modulation of FPN appeared independent of liver hepcidin mRNA expression, with no hepcidin
482 induction observed by ENTO supplementation (Figure 5L). Instead, hepcidin expression in ENTO-
483 treated ID mice dropped approximately 50-fold compared to placebo-ID mice. This may indicate
484 that ENTO treatment promotes hepcidin-suppressing signals, such as increased hypoxia or
485 erythropoietic drive, but the exact mechanism by which SYK regulates hepcidin remains to be
486 determined. On systemic levels, a 2-week ENTO treatment did not affect liver iron content within
487 IB or ID groups (Figure S5.2A) or circulating hematological parameters (Figure S5.2B-C), and it
488 only showed some tendency for the more pronounced decrease in the transferrin saturation levels

489 (Figure 5M). Therefore, we extended the period of ENTO administration for 3 weeks and evaluated
490 the systemic blood parameters. While we observed no significant difference in hemoglobin or
491 MCH between iron-restricted mice supplemented with ENTO *versus* placebo (Figure 5N, S5.2D),
492 we noticed an increase in reticulocyte counts and reduction of reticulocyte hemoglobin content
493 (Figure 5O-P), indicating the onset of systemic hematological effects of ENTO treatment.
494 Consistently, whereas erythroid progenitors' expansion was not affected by ID in the bone marrow,
495 we detected a more pronounced expansion of immature EPO-responsive splenic progenitors,
496 proerythroblasts, and EryA erythroblasts, in ENTO-treated *versus* control mice (Figure 5Q-R).
497 Consistently, plasma EPO levels were elevated in a more pronounced manner between ID and IB
498 mice following ENTO supplementation compared to placebo-exposed mice (Figure 5S).
499 Interestingly, the saturation of transferrin in the circulation was not significantly different between
500 ID mice treated with ENTO and placebo (Figure S5.2E). This suggests that a more pronounced
501 compensatory extramedullary erythropoietic response is initiated by ENTO, likely due to less
502 effective direct iron delivery from iron-recycling RPMs. Taken together, SYK activity emerged as
503 critical for the enhanced RBC-clearance capacity of RPMs in ID mice, with SYK inhibition
504 triggering compensatory erythropoietic responses that are consistent with a possible reduction in
505 iron delivery from RPMs.

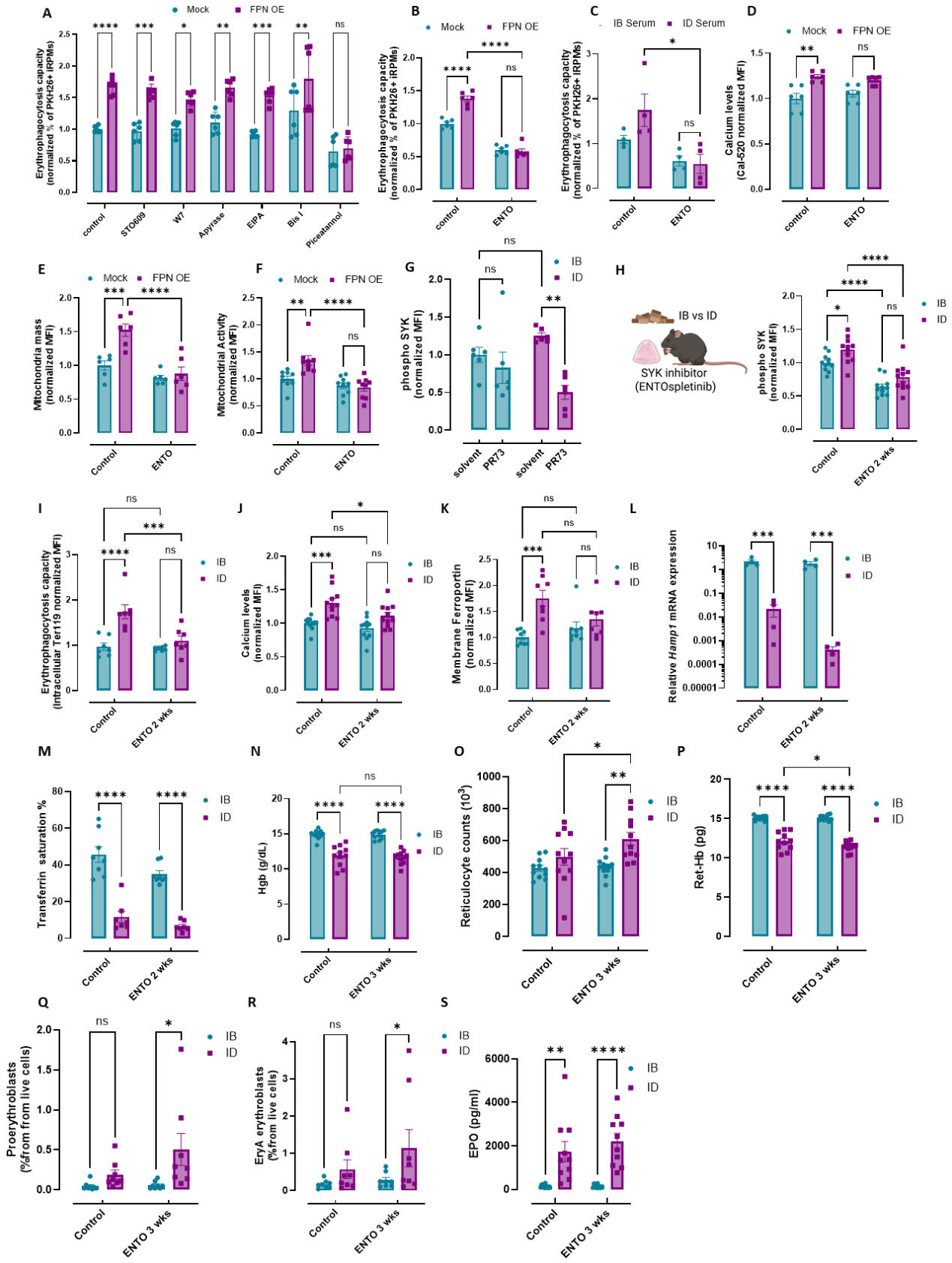
A
Mock
FPN OE
Erythrophagocytosis capacity (normalized % of PKH26+ iRPMs)
control
STO609
W7
Apyrase
EIPA
Bis I
Piceatannol
B
Mock
FPN OE
Erythrophagocytosis capacity (normalized % of PKH26+ iRPMs)
control
ENTO
C
IB Serum
ID Serum
Erythrophagocytosis capacity (normalized % of PKH26+ iRPMs)
control
ENTO
D
Mock
FPN OE
Calcium levels (Cal-520 normalized MFI)
control
ENTO
E
Mock
FPN OE
Mitochondria mass (normalized MFI)
Control
ENTO
F
Mock
FPN OE
Mitochondrial Activity (normalized MFI)
Control
ENTO
G
IB
ID
phospho SYK (normalized MFI)
solvent
PR73
solvent
PR73
H
IB vs ID
SYK inhibitor (ENTOspletinib)
IB
ID
phospho SYK (normalized MFI)
Control
ENTO 2 wks
I
IB
ID
Erythrophagocytosis capacity (Intracellular Ter119 normalized MFI)
Control
ENTO 2 wks
J
IB
ID
Calcium levels (normalized MFI)
Control
ENTO 2 wks
K
IB
ID
Membrane Ferroportin (normalized MFI)
Control
ENTO 2 wks
L
IB
ID
Relative Hamp1 mRNA expression
Control
ENTO 2 wks
M
IB
ID
Transferrin saturation %
Control
ENTO 2 wks
N
IB
ID
Hgb (g/dL)
Control
ENTO 3 wks
O
IB
ID
Reticulocyte counts (10³)
Control
ENTO 3 wks
P
IB
ID
Ret-Hb (pg)
Control
ENTO 3 wks
Q
IB
ID
Proerythroblasts (%from from live cells)
Control
ENTO 3 wks
R
IB
ID
EryA erythroblasts (%from live cells)
Control
ENTO 3 wks
S
IB
ID
EPO (pg/ml)
Control
ENTO 3 wks

506

507 **Figure 5. SYK kinase mediates the FPN-dependent adaptation of RPMs to ID conditions.**

508 (A) Normalized EP capacity of mock and FPN-iRPMs, measured by uptake of PKH26-labeled sRBCs with
509 flow cytometry. iRPMs were cultured with sRBC for 4 days before analysis and treated with inhibitors
510 targeting CaMKK (STO-609; 2.5 μM, 16 h), ATP-triggered purinergic receptor-mediated Ca^{2+} signaling
511 (Apyrase; 5U/ml, 30 min), calmodulin (W7; 20 μM, 30 min), macropinocytosis (EIPA; 25 μM, 30 min),
512 protein kinase C (Bisindolylmaleimide I, BIS I; 10 μM, 1 h), and spleen tyrosine kinase (SYK; Piceatannol;
513 100 μM, 30 min). (B) Normalized EP capacity of mock and FPN-iRPMs upon treatment with the SYK
514 inhibitor Entospletinib (ENTO) measured by uptake of PKH26-labeled sRBCs. (C) Normalized EP capacity
515 of iRPMs cultured with serum from IB or ID mice upon treatment with ENTO was measured by uptake of
516 PKH26-labeled sRBCs with flow cytometry. (D) Flow cytometric measurement of cytosolic Ca^{2+} levels in
517 mock and FPN-iRPMs upon treatment with ENTO using Cal-520 fluorescent probe. (E) Mitochondrial mass
518 was determined in mock and FPN-iRPMs upon ENTO treatment using MitoTracker Green and flow
519 cytometry. (F) Mitochondrial activity was measured in mock and FPN-iRPMs with and without treatment
520 with ENTO using the TMRE probe and flow cytometry. (G) Flow cytometric analysis of phosphorylated
521 SYK (phospho-SYK) in RPMs isolated from IB and ID mice, 4 h after intraperitoneal administration of the
522 hepcidin agonist PR73 (50 nmol/mouse). (H). IB and ID mice were supplemented with the orally
523 bioavailable SYK inhibitor ENTO via daily jelly feeding for 2 or 3 weeks before analysis (5 mg/kg/day).
524 Phospho-SYK levels in RPMs were assessed by flow cytometry in IB and ID mice supplemented with
525 ENTO. (I) EP capacity of RPMs from IB and ID mice supplemented with ENTO was determined by
526 intracellular staining for the erythrocyte marker TER119, followed by flow cytometry. (J) Cytosolic Ca^{2+}
527 levels in RPMs from IB and ID mice supplemented with ENTO were measured by flow cytometry using
528 the Cal-520 fluorescent probe. (K) Surface expression of FPN on RPMs was assessed by flow cytometry in
529 IB and ID mice supplemented with ENTO. (L) Relative mRNA expression of the Hamp gene in RPMs from
530 IB and ID mice supplemented with ENTO. (M) Plasma transferrin saturation levels were measured in IB
531 and ID mice supplemented with ENTO. (N) Blood hemoglobin (Hgb) concentration was determined in IB
532 and ID mice supplemented with ENTO. (O) Reticulocyte counts in IB and ID mice supplemented with
533 ENTO. (P) Reticulocyte hemoglobin content in IB and ID mice supplemented with ENTO. (Q and R)
534 Proerythroblast (Q) and EryA erythroblasts (R) representations in the spleens of IB and ID mice
535 supplemented with ENTO. (S) Plasma EPO levels were measured in IB and ID mice supplemented with
536 ENTO. Each dot represents either an independent cell-based experiment or one mouse. Data are represented
537 as mean ± SEM. Two-way ANOVA with Tukey's Multiple Comparison tests was used to determine
538 statistical significance. ns $p>0.05$, *$p<0.05$, **$p<0.01$, ***$p<0.001$ and ****$p<0.0001$.

539 **Functional adaptation of RPMs to iron deficiency involves enhanced BCAA catabolism and**
540 **β-oxidation pathways**

541 Efferocytosis is a continuous, energy-intensive process that demands extensive metabolic resources
542 and reprogramming[5]. Enhanced glucose uptake and potentiated OXPHOS of ID *versus* IB RPMs,
543 processes regulated in part by FPN (Figure 3N and P), have been previously reported to support
544 efferocytosis[10,11]. However, we questioned whether the metabolic reprogramming observed in
545 RPMs of ID mice reflects a unique adaptation to the challenge of processing hemoglobin-rich
546 RBCs or if it shares features with other macrophage efferocytic programs. To address this, we
547 revisited our transcriptomic and proteomic datasets. Morioka *et al*. identified nineteen solute carrier
548 (SLC) transporter genes that are transcriptionally upregulated during apoptotic cell clearance,
549 establishing a canonical efferocytosis signature[10]. Strikingly, RPMs in ID mice diverge from this

550 model: none of these nineteen SLC transporters were upregulated at the mRNA level. Similarly,
551 we observed no clear signature of hypoxia-driven programs, pentose phosphate pathway activation,
552 or increased lactate production[9,61]. Notably, RPMs also failed to display detectable protein levels
553 of key enzymes associated with amino acid signaling that support efferocytosis, including ARG1
554 and ODC1 (crucial for arginine-to-putrescine conversion), or IDO1 (the tryptophan-catabolizing
555 enzyme), and did not express SLC36A4, the principal tryptophan transporter[16,18]. While GLS1, the
556 enzyme responsible for non-canonical glutaminolysis[19], was detected through proteomic analysis,
557 its levels were unaltered under iron-deficient conditions. Conversely, the enriched category of
558 metabolic proteins differentially regulated in RPMs of ID mice revealed consistent alterations of
559 lipid metabolism, resembling other efferocytic macrophages[11]. This includes elevated enrichment
560 expression of β-oxidation enzymes, most notably the rate-limiting CPT2, induction of lipases, and
561 concurrent downregulation of DGAT1 (diacylglycerol O-acyltransferase 1), which mediates
562 triacylglyceride synthesis. Interestingly, we also observed significant enrichment of enzymes
563 involved in branched-chain amino acid (BCAA) breakdown. In parallel, two upregulated proteomic
564 hits, SLC7A7 and SLC7A8, represent antiporters that transport cationic and large neutral amino
565 acids, including BCAAs[62].

566 To validate these metabolic adaptations in RPMs of ID mice and assess whether they are specific
567 to this subset, we profiled selected proteomic hits by flow cytometry across tissue-resident
568 macrophage populations. We found that BCKDHB, the rate-limiting enzyme of BCAA catabolism,
569 the BCAA exporter SLC7A7, β-oxidation enzymes CPT2 and ACADSB, the TCA enzyme citrate
570 synthase, and the lipase ABHD12B were all significantly elevated in ID RPMs compared to iron-
571 balanced controls, while remaining unchanged or reduced in KCs and peritoneal macrophages
572 (Figure 6A). Consistently, both DGAT1 and lipid droplet levels were specifically downregulated
573 in RPMs of ID mice, suggesting a unique skewing toward energy-consuming pathways under iron
574 deficiency (Figure 6A). Next, we focused on BCAA metabolism, a pathway not previously linked
575 to enhanced efferocytosis. Baseline BCAA levels were exceptionally high in RPMs compared to
576 other splenic cell types, though still lower than in KCs and similar to peritoneal macrophages
577 (Figure 6B-C). BCAA content increased significantly in RPMs treated *ex vivo* with ERG240, a
578 pharmacologic blocker of BCAA catabolism at the stage of the first reaction catalyzed by the BCAT
579 enzyme (Figure 6C). Prolonged exposure of iRPMs to stressed RBCs, but not RBC ghosts, induced
580 strong BCKDHB expression, more robust than in standard BMDMs, and appeared to prevent

581 BCAA accumulation in RBC-exposed cells (Figure 6D-E). Notably, BCAA content remained
582 unchanged in RPMs from ID mice (Figure 6F), despite elevated EP, suggesting that BCAA
583 metabolism is tightly regulated. This implied that ID conditions impose a new metabolic
584 equilibrium necessary to maintain enhanced iron recycling by RPMs. Further exploring this
585 concept, BCKDHB levels were elevated in iRPMs overexpressing FPN, a response that, like EP,
586 depended on both FPN and SYK kinase activity (Figure 6G). The SYK dependency of BCKDHB
587 was also evident *in vivo* in RPMs derived from ID *versus* IB mice (Figure 6H). Strikingly, inhibition
588 of BCAT enzymatic activity using ERG240 abolished the EP boost caused by FPN overexpression
589 (Figure 6I), indicating that enhanced BCAA catabolism is essential for reprogramming RPM
590 phagocytic function. Similarly, exposure to leucine increased EP capacity in iRPMs in a manner
591 diminished by ERG240 pre-treatment (Figure 6J). Interestingly, BCAT inhibition also reversed
592 BCKDH induction and reduced mitochondrial mass and activity, specifically in FPN-
593 overexpressing iRPMs (Figure 6K-M). We confirmed the reversal of the enhanced phagocytic and
594 metabolic function of ID-like RPMs by BCAT suppression using another inhibitor, BAY069
595 (Figure S6.1A-C). We next looked at the requirement of β-oxidation for the RPM ID-like
596 adaptation. Like BCKDHB, CPT2 upregulation was dependent on both FPN and SYK activity
597 (Figure S6.2A). This SYK dependence was further validated *in vivo*, where ENTO reversed CPT2
598 induction in RPMs from ID mice (Figure S6.2B). Finally, inhibition of CPT2 activity with
599 trimetazidine (TMZ) abolished the enhanced EP observed with FPN overexpression, demonstrating
600 that increased β-oxidation is a key component of the metabolic programming driving augmented
601 phagocytic function in RPMs (Figure S6.2C). Taken together, both BCAA catabolism and β-
602 oxidation emerged in our study as FPN/SYK-controlled pathways that maintain enhanced
603 phagocytosis and metabolic activities of RPMs in iron deficiency.

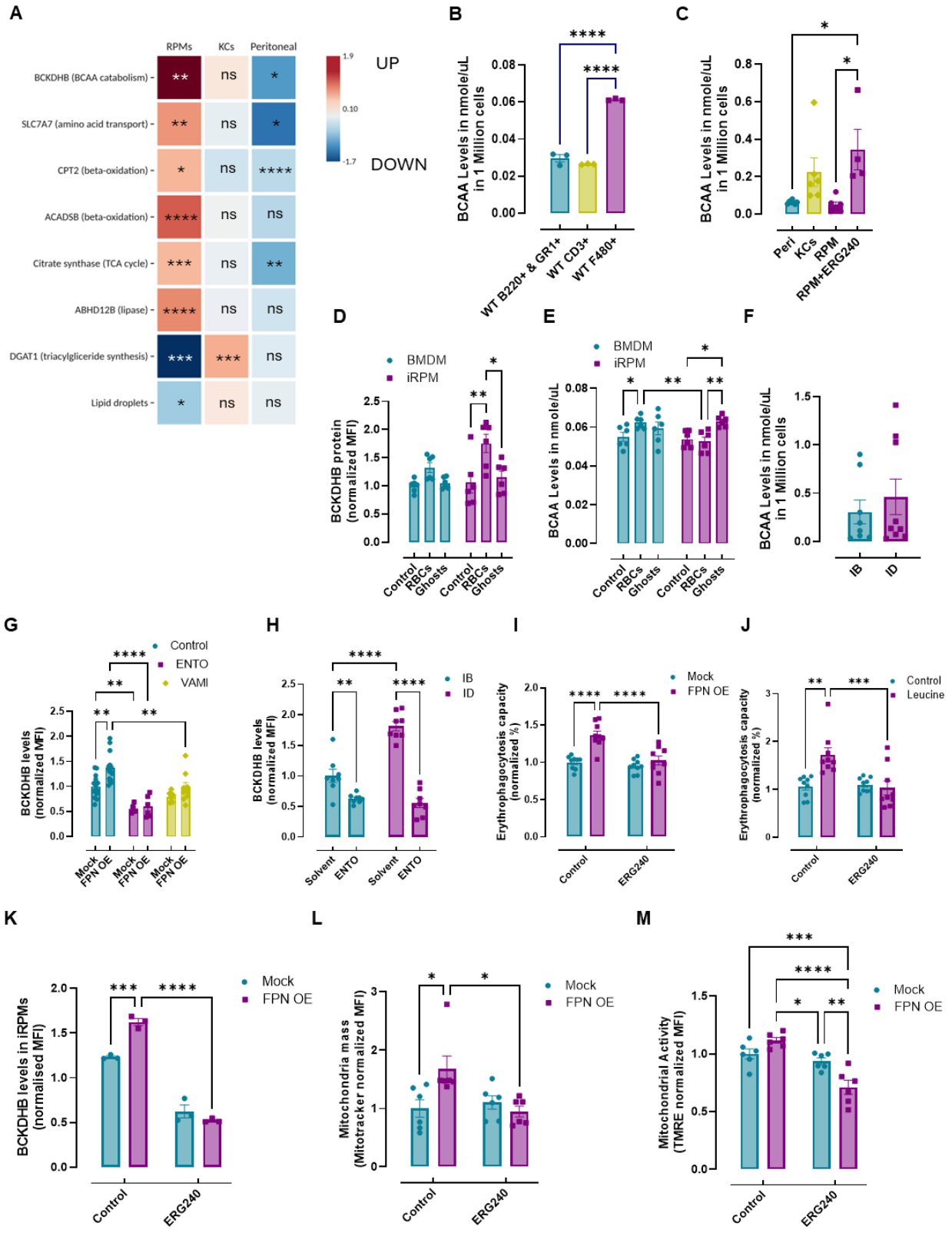
A
RPMs
KCs
Peritoneal
BCKDHB (BCAA catabolism)
SLC7A7 (amino acid transport)
CPT2 (beta-oxidation)
ACADSB (beta-oxidation)
Citrate synthase (TCA cycle)
ABHD12B (lipase)
DGAT1 (triacylgliceride synthesis)
Lipid droplets
UP
DOWN
B
BCAA Levels in nmole/uL in 1 Million cells
WT B220+ & GR1+
WT CD3+
WT F480+
C
Peri
KCs
RPM
RPM+ERG240
D
BMDM
iRPM
BCKDHB protein (normalized MFI)
Control
RBCs
Ghosts
E
BCAA Levels in nmole/uL
F
IB
ID
G
Control
ENTO
VAMI
BCKDHB levels (normalized MFI)
Mock
FPN OE
H
Solvent
I
Erythrophagocytosis capacity (normalized %)
ERG240
J
Leucine
K
BCKDHB levels in iRPMs (normalised MFI)
L
Mitochondria mass (Mitotracker normalized MFI)
M
Mitochondrial Activity (TMRE normalized MFI)

604

605

606

607 **Figure 6. Functional adaptation of RPMs to iron deficiency involves enhanced BCAA catabolism.**

608 (A) Heatmap showing levels of BCKDHB, SLC7A7, CPT2, ACADSB, citrate synthase, ABHD12B,
609 DGAT1, and lipid droplet levels across RPMs, KCs, and peritoneal macrophages measured by flow
610 cytometry. Data represent log2-transformed fold changes in cells of ID mice vs IB mice, with significant
611 changes marked by asterisks. (B) Quantification of BCAA levels in different splenic immune cell
612 populations - F4/80$^+$ RPMs, CD3$^+$ T cells, and other splenocytes, measured using a colorimetric BCAA
613 assay. (C) Quantification of BCAA levels of *ex vivo* magnetically-sorted peritoneal macrophages, KCs, and
614 RPMs (untreated and treated with ERG240). (D) Intracellular BCKDHB levels and (E) BCAA levels in
615 iRPMs and BMDMs treated with stressed RBCs and RBC ghosts compared to untreated control. (F) BCAA
616 levels in magnetically-isolated RPMs from IB and ID mice (G). Intracellular BCKDHB levels in mock and
617 FPN overexpressing (OE) iRPMs upon treatment with entospletinib (ENTO) (10 μM, 1 h) and vamifeport
618 (VAMI) (20 μM, 15 h), determined using flow cytometry (H). Intracellular BCKDHB levels in RPMs from
619 IB and ID mice supplemented with ENTO via jelly feeding (3 weeks) were determined using flow
620 cytometry. (I) Normalized EP capacity towards PKH26-sRBCs by mock and FPN overexpressing iRPMs
621 upon ERG240 treatment (10 μM, 15 h). (J) Normalized EP capacity towards PKH26-sRBCs by iRPMs upon
622 leucine exposure. (K) Intracellular BCKDHB levels in mock and FPN OE iRPMs upon treatment with
623 ERG240. (L) Mitochondrial mass was determined in mock and FPN OE iRPMs upon treatment with
624 ERG240 using MitoTracker Green and flow cytometry. (M) Mitochondrial activity was determined in mock
625 and FPN OE iRPMs upon treatment with ERG240 using the TMRE probe and flow cytometry. Each dot
626 represents one mouse or an independent cell-based experiment. Data are represented as mean ± SEM. Two-
627 way ANOVA with Tukey's Multiple Comparison tests was used in D, E, and G-M, while one-way ANOVA
628 test with Dunnett's or Tukey's Multiple Comparison tests was used in B and C, A Welch's unpaired t-test
629 determined statistical significance in A and F. ns $p>0.05$, *$p<0.05$, **$p<0.01$, ***$p<0.001$ and
630 ****$p<0.0001$.

631 ***In vivo* inhibition of BCAA catabolism alters erythrophagocytic capacity and metabolic**
632 **remodeling of RPMs in ID mice**

633 We next sought to dissect the functional relevance of BCAA metabolism in regulating
634 erythrophagocytic capacity and mitochondrial remodeling *in vivo*. First, we found that enhanced
635 OXPHOS of freshly isolated RPMs from ID mice, as measured using a Seahorse analyzer, was
636 abrogated by *ex vivo* treatment with ERG240 (Figure 7A), indicating its critical dependence on
637 BCAA catabolism. Next, we administered ERG240, a bioavailable BCAT inhibitor, to ID mice via
638 daily jelly feeding for three weeks. Consistent with our *in vitro* observations, ERG240 treatment
639 significantly suppressed the enhanced EP activity of RPMs in ID mice (Figure 7B). In parallel,
640 ERG240 administration prevented the increase of mitochondrial mass and the upregulation of
641 BCKDHB and citrate synthase protein levels, a proxy for TCA cycle capacity (Figure 7C-E).
642 Interestingly, despite this reduction in mitochondrial mass and citrate synthase, mitochondrial
643 membrane potential was not suppressed and remained comparable to untreated ID controls (Figure
644 7F), suggesting a partial uncoupling between mitochondrial polarization state and respiratory
645 functions under conditions of BCAT inhibition *in vivo*. Notably, FPN protein abundance remained

646 unchanged in ERG240-treated mice subjected to ID feeding (Figure 7G), indicating that, as in
647 ENTO-supplemented animals, reduced RPM erythrophagocytic activity is linked to diminished
648 exposure of FPN at the plasma membrane. At the systemic level, ERG240 treatment very modestly
649 affected the degree of anemia, as evidenced by a slightly more pronounced reduction in hematocrit,
650 while hemoglobin levels, MCV, and MCH values remained unchanged in ID mice receiving the
651 drug relative to untreated ID controls (Figure 7H and S7A). However, circulating reticulocyte
652 counts were significantly elevated specifically in ERG240-treated animals (Figure 7I), indicating
653 a heightened stress erythropoietic response aimed at restoring circulating red cell mass, likely
654 reflecting enhanced sensing of iron deficiency. In line with this, ERG240-treated mice displayed a
655 significant expansion of splenic erythroid progenitors, with both proerythroblasts and EryB
656 erythroblasts (Figure S7D) showing elevated representation relative to untreated ID mice.
657 Consistently, plasma EPO levels were significantly elevated in ERG240-treated ID mice (Figure
658 7J), aligning with the observed expansion of splenic erythroid progenitors. Interestingly, not only
659 were *Epo* mRNA levels elevated in the kidney of ID mice upon ERG240 supplementation as
660 compared to placebo controls, but also *Tfrc* transcription was increased (Fig. 7K and L). Similarly,
661 cardiac *Tfrc* appeared as more significantly induced in ID mice upon ERG240 treatment compared
662 with untreated ID controls, reflecting a slightly more pronounced drop in the heart non-heme iron
663 content (Fig. S7E-F). However, liver *Tfrc* induction and a decrease in iron levels upon ID diet were
664 not modified by ERG240 supplementation (Fig. S7G-H), and transferrin saturation remained
665 comparably reduced in ERG240- and placebo groups (Fig. S7I). These observations may suggest
666 sensing of more pronounced hypoxia by the kidney, and of tissue iron deficiency in some, but not
667 all, organs.

668 Finally, to assess how systemic iron deficiency alters mitochondrial fuel use *in vivo*, and how these
669 changes depend on BCAT activity, we performed MitoPlate S1 substrate profiling on freshly
670 isolated RPMs. Relative to IB controls, RPMs from ID mice exhibited broadly increased utilization
671 of glycolytic, amino-acid–derived, fatty-acid/carnitine-linked, and TCA cycle substrates,
672 consistent with their heightened OXPHOS phenotype (Figure 7M). BCAT inhibition with ERG240
673 partially attenuated this shift, most notably reducing oxidation of several TCA cycle and fatty-acid–
674 linked fuels, in line with the decrease in global mitochondrial respiration measured by Seahorse.
675 In contrast, several amino-acid substrates, such as leucine+L-malic acid, tryptamine, and ornithine,
676 remained more highly utilized than in RPMs of IB mice, indicating that while BCAT-dependent

677 BCAA metabolism contributes to the enhanced respiratory capacity of RPMs in ID mice, additional
678 metabolic pathways support the full extent of their increased mitochondrial activity.

679 Collectively, these data demonstrate that BCAA catabolism is required for sustaining increased EP
680 functions, with implications for the body's adaptation to dietary iron restriction.

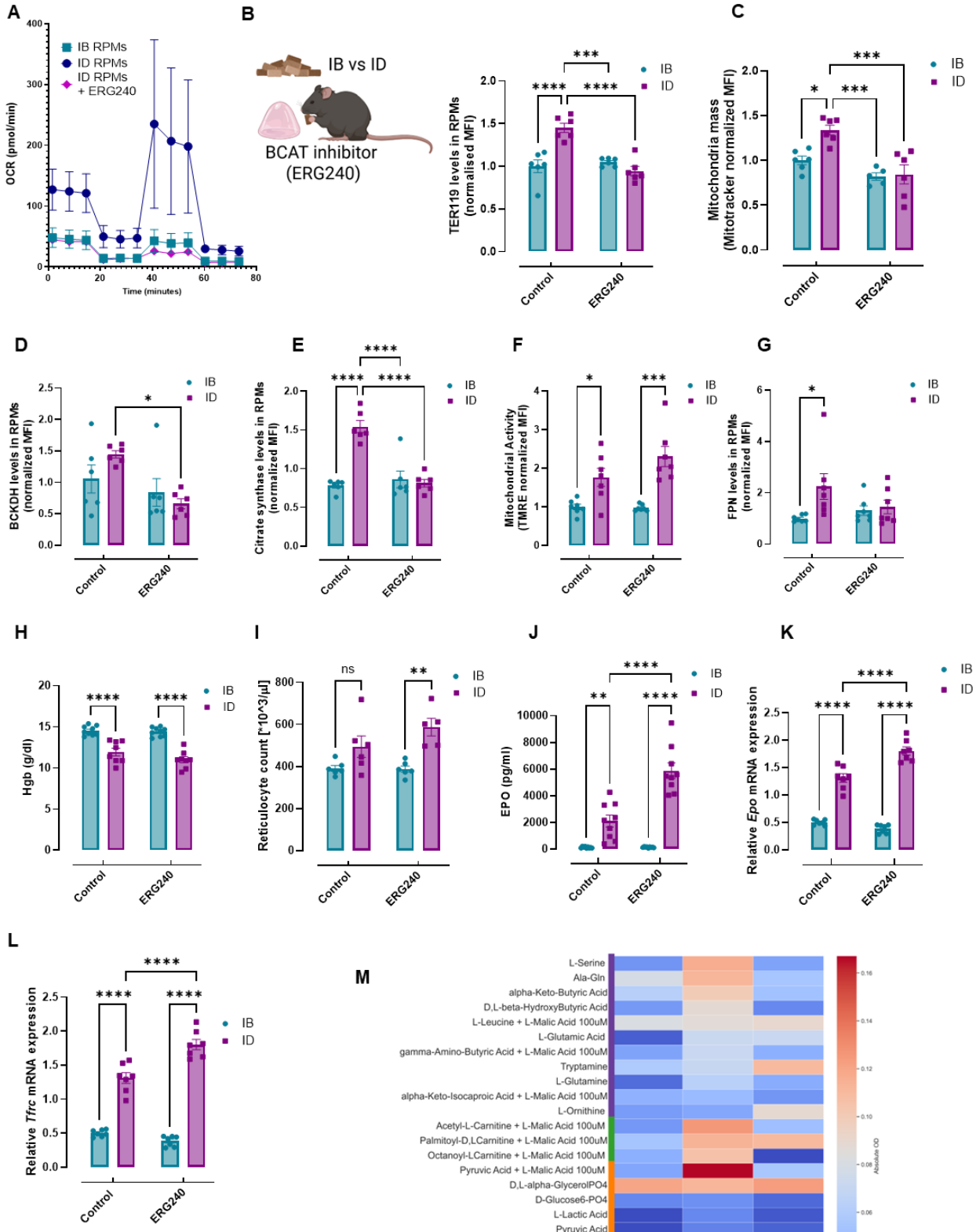
A
IB RPMs
ID RPMs
ID RPMs + ERG240
OCR (pmol/min)
Time (minutes)
B
IB vs ID
BCAT inhibitor (ERG240)
C
TER119 levels in RPMs (normalised MFI)
Mitochondria mass (Mitotracker normalized MFI)
D
BCKDH levels in RPMs (normalized MFI)
E
Citrate synthase levels in RPMs (normalized MFI)
F
Mitochondrial Activity (TMRE normalized MFI)
G
FPN levels in RPMs (normalized MFI)
H
Hgb (g/dl)
I
Reticulocyte count [*10^3/µl]
J
EPO (pg/ml)
K
Relative Epo mRNA expression
L
Relative Tfrc mRNA expression
IB
ID
Control
ERG240
M
L-Serine
Ala-Gln
alpha-Keto-Butyric Acid
D,L-beta-HydroxyButyric Acid
L-Leucine + L-Malic Acid 100uM
L-Glutamic Acid
gamma-Amino-Butyric Acid + L-Malic Acid 100uM
Tryptamine
L-Glutamine
alpha-Keto-Isocaproic Acid + L-Malic Acid 100uM
L-Ornithine
Acetyl-L-Carnitine + L-Malic Acid 100uM
Palmitoyl-D,LCarnitine + L-Malic Acid 100uM
Octanoyl-LCarnitine + L-Malic Acid 100uM
Pyruvic Acid + L-Malic Acid 100uM
D,L-alpha-GlycerolPO4
D-Glucose6-PO4
L-Lactic Acid
Pyruvic Acid
D-Gluconate6-PO4
Succinic Acid
L-Malic Acid 100uM
alpha-Keto-Glutaric Acid
L-Malic Acid
Fumaric Acid
cis-Aconitic Acid
Citric Acid
IB
ID
ID+ERG240
Absolute OD
Family
Amino acid Metabolism
Fatty acid Metabolism
Glycolysis
PPP
TCA Cycle

681

682 **Figure 7. *In vivo* inhibition of BCAA catabolism alters erythrophagocytic capacity and metabolic**
683 **remodeling of RPMs in ID mice.**

684 (A) Seahorse analysis of *ex vivo* magnetically-isolated RPMs from IB and ID mice, including 4 h ERG240
685 preincubation for RPMs from ID mice. (B) IB and ID mice were supplemented with the orally bioavailable BCAT
686 inhibitor ERG240 via daily jelly feeding for 3 weeks before analysis (5 mg/kg/day). EP capacity of RPMs from
687 IB and ID mice supplemented with ERG240, determined by intracellular staining for the erythrocyte marker
688 TER119, followed by flow cytometry. (C) Mitochondrial mass of RPMs from IB and ID mice supplemented with
689 ERG240 was determined using MitoTracker Green, followed by flow cytometry. (D) Intracellular BCKDHB
690 levels of RPMs from IB and ID mice supplemented with ERG240 (E). Intracellular citrate synthase levels of
691 RPMs from IB and ID mice supplemented with ERG240 (F). Mitochondrial activity of RPMs from IB and ID
692 mice supplemented with ERG240 was determined using the TMRE probe, followed by flow cytometry. (G) FPN
693 levels of RPMs from IB and ID mice supplemented with ERG240 were determined by flow cytometry. (H) Blood
694 hemoglobin (Hgb) and reticulocyte count (I) were determined in IB and ID mice supplemented with ERG240.
695 (J) Plasma EPO levels were measured in IB and ID mice supplemented with ERG240. (K and L) Relative mRNA
696 expression of the (K). Relative mRNA expression of *Epo* and (L) *Tfrc* genes in the kidneys of IB and ID mice
697 supplemented with ERG240 (M). Absolute mitochondrial substrate utilization profiles of RPMs from IB, ID, and
698 ID mice supplemented with ERG240, measured using the MitoPlate S1 assay. Blank-corrected OD values for all
699 metabolites with detectable activity in ID RPMs (n = 27) are shown and grouped by metabolic pathway. Each
700 dot represents one mouse or an independent cell-based experiment. Data are represented as mean ± SEM. Two-
701 way ANOVA with Tukey's Multiple Comparison tests was used in B-L. ns $p>0.05$, *$p<0.05$, **$p<0.01$,
702 ***$p<0.001$ and ****$p<0.0001$.

703

704 ## Discussion

705 Iron deficiency is a complex physiological state with multifaceted implications. The precise
706 quantitative thresholds that trigger cellular or organismal functional consequences, and the cell-
707 type-specific molecular consequences, including the identification of the most vulnerable cell types
708 and the sequence of cellular dysfunction triggered by iron deficiency, remain poorly understood.
709 Beyond its well-known erythropoietic effects leading to anemia, iron deficits impair neuronal and
710 muscle functions[33,63,64], suppress immune cell activity and proliferation[65–68], and dysregulate
711 macrophage responses[49,50,69,70]. However, the seemingly contradictory findings regarding the
712 effects of iron depletion on macrophage inflammatory cytokine production *in vitro* versus *in*
713 *vivo*[49,50,69,70] highlight the critical need for a more precise, cell-type-specific, and context-dependent
714 understanding of how low iron status affects macrophage functions. Specifically, how RPMs,
715 specialized iron-recycling cells central to the maintenance of systemic iron homeostasis, adapt to
716 the metabolic stress of systemic iron deficiency remains a key open question. Here, we address this
717 gap by defining a signaling-metabolic circuit through which systemic iron deficiency reprograms
718 RPMs to enhance erythrophagocytosis and sustain iron recycling (Fig. 8).

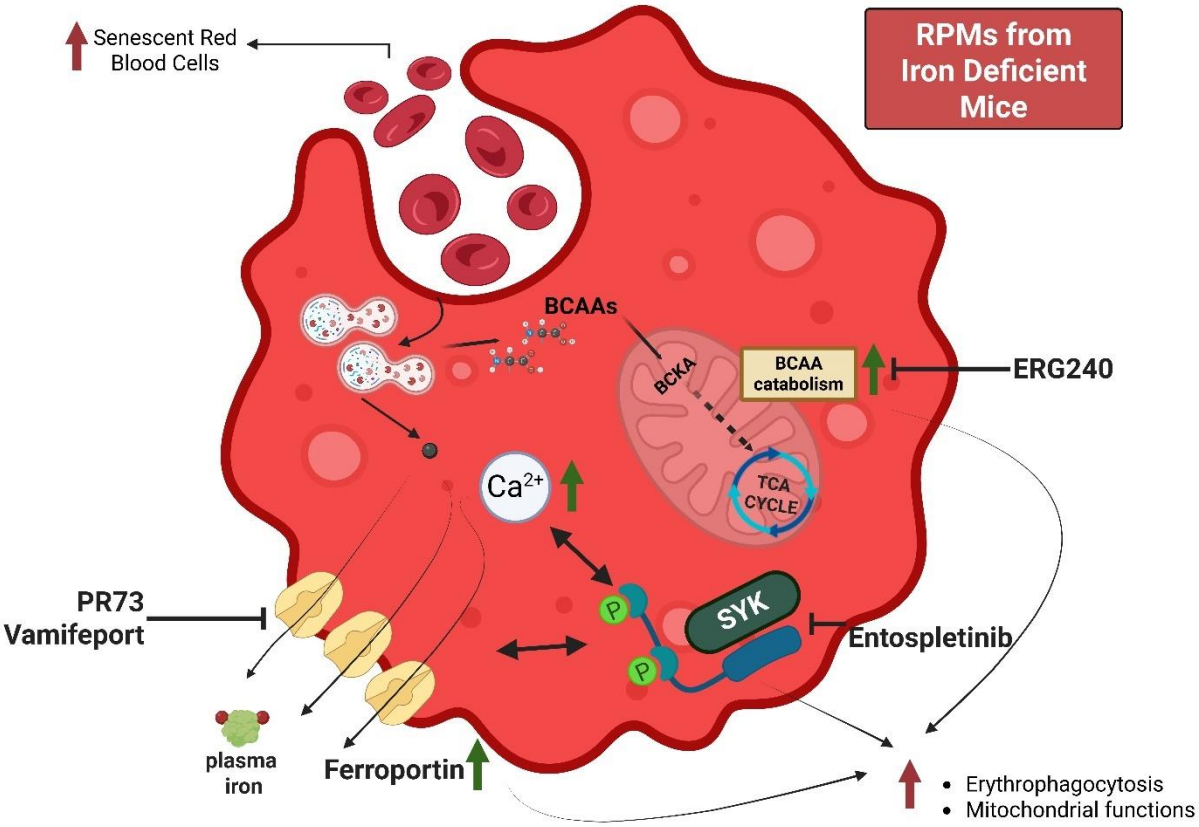

Figure 8. Iron deficiency induces metabolic rewiring of red pulp macrophages to enhance erythrophagocytosis.

Model illustrating how systemic iron deficiency reprograms RPMs to sustain iron recycling. Increased FPN-mediated iron export activates SYK-dependent signaling, promoting mitochondrial metabolic adaptation, including BCAA catabolism, which supports enhanced erythrophagocytosis of senescent RBCs. Pharmacological inhibition of FPN, SYK, or BCAA catabolism disrupts this adaptive program.

RPMs from ID mice displayed classical markers of cellular iron depletion (increased TFR1, decreased ferritin), reflecting activation of the iron-responsive element/iron regulatory protein (IRE/IRP) system, a post-transcriptional regulatory mechanism that normally increases iron uptake and reduces iron storage and FPN-mediated export under iron-limiting conditions[20,25]. However, we observed increased FPN expression in RPMs of ID mice, despite proteomic analysis showing elevated IRP2 levels. This implies that suppressed hepcidin levels in iron deficiency, which relieve the dominant negative regulation of FPN, override any potential IRP2-mediated repression. Although RPM iron stores were low in ID mice, increased LIP and oxidative stress were observed relative to IB controls, consistent with enhanced EP activity and a likely increase in cellular iron flux. Intriguingly, this observation suggests that other iron-related signals beyond LIP contribute to IRP2 stabilization in RPMs. The elevated FPN expression facilitates the export of iron derived

737 from engulfed RBCs, likely supporting the accelerated stress erythropoiesis in the spleen and the
738 iron needs of other cell types during iron deficiency. These results reveal an adaptive mechanism
739 in RPMs that prioritizes systemic iron delivery while promoting more efficient clearance of
740 senescent RBCs in the spleen in response to dietary iron deficiency. Importantly, by demonstrating
741 that the RBC clearance capacity of RPMs in ID mice depends on functional FPN, our findings
742 highlight a tight coordination between iron export and its delivery through erythrophagocytosis,
743 representing, to the best of our knowledge, a previously unrecognized concept. The relatively mild
744 systemic effects observed upon disruption of these adaptive mechanisms may reflect the short-term
745 nature of their experimental inhibition in RPMs. Nevertheless, our findings underscore the need to
746 determine how RPM rewiring and increased EP during iron deficiency reshape tissue iron
747 distribution, and how these metabolic and functional adaptations ultimately influence organismal
748 physiology, including immune competence, neuronal function, and muscle performance.

749 The established cellular response to iron deficiency, observed in iron-deprived macrophages *in*
750 *vitro* and in TFR1-null cardiomyocytes, involves a metabolic shift toward glycolysis accompanied
751 by mitochondrial dysfunction and impaired electron transport chain activity[49,71]. In contrast, RPMs
752 from ID mice show enhanced mitochondrial function, with increased mitochondrial mass and
753 elevated OXPHOS activity confirmed by Seahorse and proteomic analyses, accompanied by an
754 increase in mitochondrial membrane potential. This unique, cell-type-specific metabolic
755 adaptation, absent in Kupffer cells and peritoneal macrophages, suggests that RPMs are exceptional
756 in adjusting their physiology to increased bioenergetic demand, imposed by boosted iron recycling
757 capability. Whether these responses are driven by the spleen's unique microenvironment,
758 potentially via signals from extramedullary erythropoiesis, remains to be understood. Importantly,
759 this exceptional metabolic state of highly enhanced mitochondrial respiration was acutely shut
760 down by inhibition of FPN with PR73, and mirrored by suppressed glucose uptake and protein
761 synthesis *in vivo*, pointing to a novel relationship between FPN functionality and cellular
762 metabolism in the context of heightened efferocytic activity. These findings were further supported
763 by the similar metabolic features induced solely by FPN overexpression in the RPM *in vitro* model.

764 Emerging evidence links substantial metabolic reprogramming to efferocytosis. This is hallmarked
765 by altered amino acid utilization, particularly of arginine[16], methionine[17], tryptophan[18], and
766 glutamine[19], lactate production[9,10], boosted pentose phosphate pathway[14,15], increased glucose
767 uptake and glycolysis[9,10], fatty acid oxidation[11], and, critically, enhanced mitochondrial

768 respiration[12,13], acting in concert to sustain energetically demanding efferocytosis and promote an
769 anti-inflammatory milieu[12,13]. While RPMs of ID mice retain some of these metabolic traits,
770 particularly enhanced OXPHOS, our omics analyses reveal a distinct divergence from canonical
771 efferocytic programs. For example, key transporters and enzymes involved in arginine, tryptophan,
772 and glutamine metabolism are absent or uninduced. BCAAs represent important metabolic
773 substrates for macrophages, fueling the TCA cycle and supporting both pro-inflammatory and anti-
774 inflammatory polarization in a context-dependent manner[72–74]. However, the relevance of BCAA
775 catabolism in promoting efferocytosis and controlling the functions of iron-recycling macrophages
776 has remained largely unexplored. Our study demonstrates that RPMs of ID mice uniquely
777 upregulate BCKDHB in a manner controlled by both FPN and SYK, identifying the new
778 mechanistic link between the capacity of BCAA breakdown and these regulators. We further show
779 that enhanced RBC clearance in RPMs relies on BCAA-driven bioenergetics, reflected by the
780 dependence of their heightened OXPHOS on BCAT activity. The MitoPlate profiling further
781 clarifies this metabolic specialization. Although RPMs from ID mice display broadly elevated
782 mitochondrial substrate use, BCAT inhibition led to a marked divergence between fuel classes:
783 oxidation of several key TCA cycle and fatty-acid-linked substrates was substantially reduced by
784 ERG240, whereas utilization of select amino-acid-derived fuels, particularly leucine, malic acid,
785 tryptamine, and ornithine, remained comparatively resilient. This pattern points to a reliance on
786 non-canonical transamination-linked anaplerosis that sustains the α-ketoglutarate (α-KG) pool.
787 When BCAT is suppressed, the diminished α-KG supply limits TCA cycle flux, making
788 conventional carbon inputs more vulnerable, while specific amino acid pathways able to restore or
789 utilize α-KG through distinct enzymatic routes can still support the elevated mitochondrial state
790 characteristic of RPMs in ID mice. Altogether, these findings reveal either a previously
791 unrecognized specialization of RPMs for processing BCAA-rich RBCs or suggest a more general,
792 therapeutically exploitable metabolic dependency in efferocytic macrophages. Future work will
793 clarify whether this pathway is restricted to RPMs or is required for efficient or increased clearance
794 of apoptotic cells in other macrophage subtypes.

795 Our work further identified significantly elevated intracellular Ca^{2+} levels in RPMs of ID mice,
796 closely dependent on functional FPN and correlating with their enhanced EP capacity. While recent
797 studies have demonstrated that PKC activity can promote FPN exposure on the cell surface in type
798 2 diabetes and as a response to iron loading[75], our findings suggest that, in the context of iron

799 deficiency, increased FPN expression and elevated intracellular Ca^{2+} may represent parallel or
800 intersecting pathways that together facilitate enhanced EP. It is also plausible that RPMs of ID
801 mice, characterized by low iron stores but elevated LIP, additionally regulate FPN exposure on the
802 surface via Ca^{2+}-stimulated high PKC activity. Our data suggest no direct involvement of PKC in
803 mediating FPN-dependent and Ca^{2+}-triggered regulation of EP, at least using the cellular model of
804 RPMs. However, RPMs of ID mice treated by ENTO not only downmodulate EP but also FPN
805 surface levels and Ca^{2+}, which may represent a secondary response, possibly mediated by PKC
806 activity.

807 Our discovery that SYK drives EP in RPMs aligns with its emerging roles in diverse phagocytic
808 processes. Bian *et al*. demonstrated that SYK activation overrides Cd47-SIRPα-mediated "don't
809 eat me" signals to enable inflammation-driven clearance of "self" RBC[30]. Recent studies highlight
810 SYK as a critical mediator of microglial responses to amyloid-β (Aβ) plaques in Alzheimer's
811 disease, where SYK deficiency impairs Aβ phagocytosis[76,77]. Our work extends this observation
812 by identifying iron deficiency as a physiological trigger for SYK activation in RPMs, with
813 upstream regulation by the low hepcidin-high FPN. Furthermore, our work reveals SYK-dependent
814 metabolic-phagocytic coupling. Whereas previous findings link high SYK activity to inhibition of
815 mitochondrial respiration[78], we show that mitochondrial membrane potential and mass, heightened
816 by FPN overexpression, critically depend on SYK activity. Critically, our data imply that SYK may
817 represent a novel molecular switch for the regulation of efferocytic capacity, a concept that requires
818 further work.

819 Finally, the FPN–SYK-mediated rewiring of RPMs in iron deficiency does not resemble M1/M2-
820 like polarization. RPMs from ID mice exhibited an ambiguous pattern of surface marker
821 alterations, indicating no consistent pro- or anti-inflammatory skewing, and no clear regulation of
822 immune-linked mediators in omics data. They also employed a mixed functional phenotype:
823 elevated ROS production, driven by increased labile iron, characteristic of M1 macrophages,
824 alongside enhanced oxidative phosphorylation, mitochondrial biogenesis, and lysosomal activity,
825 features typically associated with M2 macrophages[79–85]. Likewise, SYK has emerged as a context-
826 dependent regulator of macrophage polarization and function, promoting fibrotic and
827 proinflammatory programs in diabetic kidney disease and ulcerative colitis, respecitvely and
828 enabling immunosuppressive reprogramming of tumor-associated macrophages[86,87,88]. Together
829 with the notion that enhanced EP in RPMs only partially resembles previously reported adaptation

830 mechanisms to efferocytosis, our work proposes that the polarization state of RPMs in iron
831 deficiency represents a new type of adaptation, whose resemblance in other macrophage
832 types/environmental conditions opens an avenue for future investigations.

833 **Methods**

834 **Mice**

835 Female C57BL/6 J mice were utilized for the experiments and housed under specific pathogen-free
836 (SPF) conditions at the Experimental Medicine Centre in Bialystok, Poland. These mice were
837 provided with either a standard iron-balanced diet (200 mg/kg, SAFE U8958P; IB diet) or an iron-
838 deficient diet (5.9 mg/kg, SAFE U8958P; ID diet) for 5 weeks, commencing at 4 weeks of age. 9-
839 week-old *Tmprss6* wild-type and KO mice were provided by Dr. Delphine Meynard from
840 INSERM, Toulouse, France. Upon arrival at the local facility at the International Institute of
841 Molecular and Cell Biology (IIMCB), mice were acclimatized briefly before being sacrificed or
842 subjected to further procedures, if required. Ms4a3-Cre mice were obtained from Florent
843 Ginhoux[43], and RosaTdT reporter mice [B6;129S6-Gt(ROSA)26Sortm9(CAG-tdTomato)Hze/J
844 JAX#: 007905] were a kind gift of Agnieszka Kobielak. Female C57BL/6-Tg(UBC-GFP)30Scha/J
845 (UBI-GFP/BL6) mice were kindly provided by Aneta Suwińska (Faculty of Biology, University of
846 Warsaw, Poland). For primary cell cultures, C57BL/6 J mice were maintained in the SPF facility
847 at the Mossakowski Medical Research Institute in Warsaw, Poland.All animal experiments and
848 protocols were approved by the respective local ethical committees in Olsztyn and Warsaw,
849 including the decisions: Uchwala 026, WAW2/015/2019, and WAW2/048/2020). Usage of
850 Ms4a3Cre-RosaTdT reporter mice was approved by WAW2/126/2023. For PR73 administration,
851 mice were intraperitoneally injected with 50 nmol of PR73 for 4 h before being sacrificed. The
852 procedure was approved by the local ethical committee in Warsaw (WAW2/150/2019).
853 Experiments including SYK and BCAA catabolism suppression were covered by the permissions:
854 WAW2/068/2024 and WAW2/029/2025.

855 **Isolation of Single-Cell Suspensions from Murine Organs**

856 Bone marrow cells were obtained by flushing the femurs and tibias with sterile HBSS (Gibco,
857 14025092) using a 25G needle. Following centrifugation at 600 x g for 10 min at 4°C, the pellet
858 containing the isolated cells was collected for further processing. The spleen was harvested and
859 homogenized by passage through a 70 µm cell strainer (pluriSelect, 43-50070-51). Before FACS
860 sorting, the spleen was enzymatically digested with HBSS containing 1 mg/mL Collagenase D

861 (Roche, 11088882001) and 50 U/mL DNase I for 30 min at 37°C to facilitate cell dissociation. The
862 resulting cell suspension was then washed with cold HBSS and centrifuged at 600 x g for 10 min
863 at 4°C. The harvested liver was perfused using Liver Perfusion Medium (Gibco, 17701038),
864 followed by mincing and enzymatic digestion in Liver Digest Medium (Gibco, 17703034) at 37°C
865 for 30 min. The digested liver tissue was then pressed through a 70 μm strainer into HBSS. The
866 resulting cell suspension was centrifuged at 50 g for 3 min to separate the hepatocyte-enriched
867 pellet, which was discarded. The supernatant, containing non-parenchymal cells, was further
868 centrifuged at 700 g for 15 min at 4°C. The resulting cell pellet was resuspended in a solution of 5
869 mL PBS with 0.5% BSA and 5 mL of 50% Percoll (Cytiva, 17-0891-01) diluted in PBS. This
870 suspension underwent Percoll gradient centrifugation at 700 g for 30 min at 20°C to enrich specific
871 cell populations. The peritoneal cavity was lavaged with HBSS to collect peritoneal fluid. The
872 retrieved fluid was then passed through a 70 μm strainer to remove debris, followed by
873 centrifugation at 600 x g for 10 min at 4°C to pellet the peritoneal cells. Blood was collected via
874 cardiac puncture into a heparin-coated tube. The cells were separated by centrifugation at 400 g for
875 10 min at 4°C following a wash with HBSS. RBCs present in a single-cell suspension were lysed
876 using 1X RBC Lysis buffer (BioLegend, 420302) for 3 min at room temperature. However, this
877 step was excluded when analyzing erythroid cells and RBCs. Following that, the cells were washed
878 with 1X HBSS and centrifuged at 600g for 10 min at 4°C. The resulting pellet was processed for
879 subsequent functional assays and antibody labeling.

880 **Generation of iRPMs**

881 Mononuclear cells were aseptically harvested from the femurs and tibias of mice and subsequently
882 cultured at a concentration of 0.5×10^6/1mL in RPMI-1640 medium (Gibco, 61870036)
883 supplemented with 10% FBS (Cytiva, SV30160.03), 1X Penicillin-Streptomycin (Gibco,
884 15140122), and 20 ng/mL of macrophage colony-stimulating factor (MCSF, BioLegend, 576406)
885 in a 5% CO_2 incubator at 37°C. On days 4 and 6 of culture, the medium was replaced with fresh
886 complete medium supplemented with 20 μM hemin (Sigma-Aldrich, 51280). In the initial
887 experiments, we also included 10 ng/mL interleukin-33, which was later omitted as it was not
888 critical for mimicking RPM-like phenotypes. All experiments were performed on day 8 of culture.
889 For treatments, hemin (Sigma-Aldrich, 51280) solution was prepared with 0.15 M NaCl containing
890 10% NH_4OH. For the phagocytosis assay, iRPMs were treated for 1 h with 10 μM
891 Entospletinib (Selleck, S7523), 15 h with 10 μM ERG240 (MedChemExpress, HY-W193545A),
892 15 h with 10μM BAY-069 (MedChemExpress, HY-148242), 15 h with 10 mM leucine (Sigma-

893 Aldrich, L8000), 24 h with 100 μM deferoxamine (DFE, Sigma-Aldrich, D9533), 30 min with 10
894 μM BAPTA/AM (CALBIOCHEM, 196419), 1 h with 3 mM EGTA (Sigma, E8145), 16 h with 2.5
895 μM STO609 (Sigma-Aldrich, S1318), 30 min with 20 μM W7 (Sigma-Aldrich, 681629), 30 min
896 with 5U/ml apyrase (Sigma-Aldrich, A6535), 30 min with 25 μM EIPA (Selleckchem, S9849), 1 h
897 with 10 μM BisindolylmaleimideI (Sigma-Aldrich, 203290), 30 min with 100 μM Piceatannol
898 (Sigma-Aldrich, P0453). Vamifeport was a kind gift from CSL Vifor and was purchased from
899 MedChem Express (VIT-2763), and was used for 15 h at 20 μM concentration.

900 **Flow Cytometric Analysis and Cell Sorting**

901 Cell suspensions of spleens and livers at a concentration of approximately 1×10^7, along with
902 iRPMs, were stained with LIVE/DEAD Fixable Aqua/Violet (Invitrogen, L34966/L34964)
903 following the manufacturer's instructions to identify dead cells. After extensive washing, Fc block
904 was added to the cells at a 1:100 dilution in FACS buffer and incubated at 4˚C for 10 min. The cells
905 were then stained with fluorophore-conjugated antibodies at a dilution of 1:100 to 1:400, depending
906 on the titration, in FACS buffer for 30 min at 4˚C. The cells were washed thoroughly with FACS
907 buffer and analyzed using flow cytometry. For the analysis of splenic RPM populations, cells were
908 initially identified as $CD45^+$ $F4/80^{high}$ $CD11b^{dim}$ $TREML4^+$ after excluding lineage-positive cells
909 ($CD3^+$ T cells, $B220^+$ B cells, Gr-1^+ neutrophils/monocytes), as previously described[27]. However,
910 since we observed that the majority of RPMs were $TREML4^+$, we omitted TREML4 from the panel
911 in further analyses. Surface antibodies against CD45 (Biolegend, 30-F11), CD45R/B220
912 (Biolegend, RA3-6B2), Ly-6G/Ly-6C (Gr-1) (Biolegend, RB6-8C5), CD3 (Biolegend, 17A2),
913 F4/80 (Biolegend, BM8), CD11b (Biolegend, M1/70), and TREML4 (Biolegend, 16E5) were used.
914 For erythroid cell analysis, TER-119 (Biolegend) and CD71 (Biolegend, RI7217) were included.
915 Staining for proteins linked to amino acid and lipid metabolism utilized antibodies against
916 BCKDHB (Santa Cruz Biotechnology, sc-374630), SLC7A7 (Invitrogen, PA5-113527), CPT2
917 (Novus Biologicals, NBP1-85471), ACADSB (Proteintech, 13122-1-AP), ABHD12B
918 (Proteintech, 20623-1-AP), citrate synthase (Proteintech, 16131-1-AP), and DGAT1 (Novus
919 Biologicals, NB110-41487). The analysis of liver KCs and iRPM populations involved the use of
920 surface antibodies, including CD45 (Biolegend, 30-F11), F4/80 (Biolegend, BM8), and CD11b
921 (Biolegend, M1/70). FPN detection was performed using a non-commercial antibody that
922 recognizes the extracellular loop of mouse FPN (rat monoclonal, Amgen, clone 1C7) directly
923 conjugated with Alexa488 (Alexa Fluor 488 Labeling Kit ab236553). To analyze RBCs, surface
924 antibodies such as CD45 (Biolegend, 30-F11), TER-119 (Biolegend), and CD71 (Biolegend,

925 RI7217) were used. Lastly, the analysis of peritoneal macrophages involved the use of surface
926 antibodies, including CD45 (Biolegend, 30-F11), F4/80 (Biolegend, BM8), MHCII (Biolegend,
927 M5/114.15.2), and CD11b (Biolegend, M1/70). Events were acquired using Aria II (BD
928 Biosciences) or CytoFLEX (Beckman Coulter) and were analyzed using FlowJo or CytExpert,
929 respectively. For RNA sequencing (RNA-seq) and ATP levels quantification, RPMs were sorted
930 into Trizol-LS (Invitrogen, 10296010) or assay buffer, respectively, using an Aria II cell sorter (BD
931 Biosciences) with an 85 μm nozzle.

932 **Functional Assays and Detection of Intracellular Fe^{2+} Iron**

933 To assess intracellular ROS levels, CellROX Deep Red Reagent (Invitrogen, C10422) was used,
934 and fluorescence was measured in the APC channel following the manufacturer's protocol. The
935 lysosomal activity was evaluated using the Lysosomal Intracellular Activity Assay Kit (Biovision,
936 K448) and fluorescence was measured in the FITC channel as directed by the manufacturer. To
937 measure mitochondrial activity, the tetramethylrhodamine ethyl ester (TMRE) fluorescent probe
938 (Sigma-Aldrich, 87917) was utilized at a concentration of 400 nM for 30 min at 37 °C, and the
939 fluorescence was measured in the PE channel. Mitochondrial mass was measured by fluorescence
940 levels upon staining with MitoTracker Green (Invitrogen, M7514) at 100 nM for 30 min at 37 °C
941 in the FITC channel. Intracellular calcium (Ca^{2+}) levels were assessed using the Cal-520 AM probe
942 (Abcam, ab171868) at 5 μM for 1 h at 37 °C. Briefly, surface-stained cells were incubated with the
943 probe in HBSS, followed by immediate flow cytometric analysis in the FITC channel without
944 further washing. Intracellular ferrous iron (Fe^{2+}) was quantified using FerroOrange (Dojindo, F374)
945 with detection in the PE channel by flow cytometry. Surface-stained cells were incubated in HBSS
946 containing 1 μM FerroOrange for 30 min at 37 °C and immediately analyzed without further wash
947 steps. Lipid droplet content was quantified using the Lipid Droplet Assay Kit Deep Red (Dojindo,
948 LD06-10) following the manufacturer's protocol, with fluorescence recorded in the APC channel.
949 Glucose uptake was measured using the Glucose Uptake Capacity Assay Kit (Dojindo, UP03), and
950 fluorescence was measured in the APC channel as per the manufacturer's protocol. To perform
951 intracellular staining, cells that had already been surface-stained were fixed using 4% PFA and
952 permeabilized with 0.5% Triton-X in PBS. The cells were then stained with appropriate primary
953 antibodies for 1 h at 4°C, followed by a 30-minute incubation with Alexa Fluor 488 or Alexa Fluor
954 647 conjugated anti-Rabbit IgG (1:1000 Thermo Fisher, A-21206). Afterward, the geometric mean
955 fluorescence intensities (MFI) of the probes/target protein levels were measured by flow cytometry
956 using Aria II (BD Biosciences) or CytoFLEX (Beckman Coulter). Data were then analyzed using

957 FlowJo or CytExpert software, respectively. The MFI of the adequate fluorescence minus one
958 (FMO) control was subtracted from the samples' MFI to quantify the data. The data were further
959 normalized for analysis.

960 **ATP levels**

961 The levels of cellular ATP in FACS-sorted RPMs (10000 cells per sample) were measured using
962 the ATP Assay Kit (Sigma-Aldrich, MAK473) according to the manufacturer's instructions.

963 **Magnetic Sorting of RPMs**

964 60 x 10^6 cells were incubated for 15 min at 4°C in PBS containing 5% Normal Rat Serum (Thermo
965 Scientific, 10710C) and anti-CD16/32 antibody (Biolegend, 101320) in a 5 mL round-bottom tube.
966 The cells were then labeled with anti-F4/80 (APC, Biolegend, 123116), anti-Ly-6G/Ly-6C (Gr-1)
967 (Biotin, Biolegend, 108403), anti-CD3 (Biotin, Biolegend, 100243), anti-mouse Ly-6C (Biotin,
968 Biolegend, 128003), and anti-B220 (Biotin, Biolegend, 103204) for 20 min at 4°C in the dark. The
969 cells were washed with a cold PBS solution containing 2 mM EDTA and 0.5% BSA (hereafter
970 referred to as "sorting buffer") and centrifuged at 600 g for 10 min. The pellet was resuspended in
971 400 µL of sorting buffer containing 50 µL of MojoSort Streptavidin Nanobeads (Biolegend,
972 480016) and kept in the cold and dark for 15 min. After incubation, an additional 400 µL of sorting
973 buffer was added to the cells, and the tube was placed on an EasyEights EasySep Magnet
974 (STEMCELL, 18103) for 7 min. The supernatant was transferred to a fresh 5 mL tube and
975 centrifuged at 600 g for 10 min. The pellet was resuspended in 100 µL of sorting buffer, and 10 µL
976 of MojoSort Mouse anti-APC Nanobeads (Biolegend, 480072) were added. The suspension was
977 gently pipetted and incubated for 15 min at 4°C in the dark. The tube was then placed on a magnet
978 for 7 min, and the supernatant was saved for analysis. The beads with attached F4/80+ cells were
979 washed with sorting buffer and counted under a light microscope with a Neubauer chamber. The
980 cells were pelleted and frozen in liquid nitrogen for further analysis.

981 **Magnetic Sorting of RBCs, T Cells, B Cells, Granulocytes, Peritoneal Macrophages, and**
982 **Kupffer Cells**

983 RBCs, T cells, B cells, and granulocytes were magnetically isolated from spleen using the same
984 general workflow as described for splenic RPM isolation, with modified antibody labeling and
985 bead combinations. Single-cell suspensions were incubated with anti-CD16/32 to block Fcγ
986 receptors on leukocytes prior to staining. Cells were stained with biotinylated antibodies against
987 TER-119 (RBCs), B220 (B cells), and Gr-1 (granulocytes) and a PE-conjugated anti-CD3 antibody

988 (T cells) Biotin-labeled RBCs, B cells, and granulocytes were isolated using streptavidin
989 Nanobeads, and $CD3^+$ T cells using anti-PE Nanobeads. This strategy yielded highly purified
990 fractions of RBCs, T cells, B cells, and granulocytes for downstream analyses. Peritoneal
991 macrophages were isolated using the same marker and bead strategy as splenic macrophages, with
992 biotinylated antibodies against CD3, B220, and Gr-1 for lineage depletion, followed by positive
993 selection of $F4/80^+$ cells using anti-APC nanobeads.

994 Magnetic sorting of Kupffer cells was performed according to a two-step liver perfusion protocol
995 with minor modifications. Briefly, mice were euthanized, and livers were perfused in situ through
996 the inferior vena cava with Liver Perfusion Medium for 3 min, followed by perfusion with
997 prewarmed Liver Digest Medium for 15–20 min after transection of the portal vein. Digested livers
998 were gently dissociated in RPMI 1640, filtered through a 100-µm strainer, and subjected to two
999 rounds of low-speed centrifugation (50 g, 3 min) to remove hepatocytes. The resulting non-
1000 parenchymal cell fraction was centrifuged at 650 g for 15 min at 4 °C, treated with red blood cell
1001 lysis buffer, and further purified using a two-layer Percoll gradient. Cells collected from the
1002 interphase between 25% and 50% Percoll were washed, Fc-blocked, and incubated with anti-F4/80
1003 MicroBeads UltraPure. $F4/80^+$ Kupffer cells were isolated using magnetized LS separation
1004 columns, washed, and prepared for downstream analyses. All cell isolations were performed at 4
1005 °C, and purified cells were counted, pelleted, and snap-frozen in liquid nitrogen prior to
1006 intracellular BCAA quantification.

1007 **Measurement of Cellular Iron Levels**

1008 To determine the levels of total iron in magnetically sorted RPMs, the Iron Assay Kit from Sigma-
1009 Aldrich (MAK025) was employed by following the manufacturer's instructions. The volume of
1010 buffers and reagents used in the measurement of total iron in RPMs was adjusted accordingly. The
1011 absorbance at 593 nm was recorded using a Nanodrop ND-1000 Spectrophotometer from Thermo
1012 Fisher Scientific. Iron concentrations in RPMs (ng/µL) were calculated from the standard curve
1013 and then normalized to the number of cells in each sample.

1014 ***In Vivo* RBC Lifespan**

1015 A sterile solution of EZ-Link Sulfo-NHS Biotin (Thermo Fisher Scientific, 21217) was prepared
1016 in PBS with a final concentration of 1 mg per 100 µL. The solution was then filtered through a 0.1
1017 µm filter (Millipore, SLVV033RS). One day before the first blood collection, 100 µL of the sterile
1018 Biotin solution was intravenously injected into the mice. Blood samples were collected from the

1019 tail vein on days 0, 5, 12, 16, and 21, using heparinized capillaries to prevent clotting. RBCs were
1020 separated by centrifugation at 400 g for 5 min at 4°C, and each sample was resuspended in 250 μL
1021 of HBSS containing 5% normal rat serum (Thermo Fisher Scientific). The suspension was then
1022 mixed with 2 μL of fluorescently labeled anti-TER-119 and streptavidin, except for the
1023 fluorescence minus one (FMO) sample in each group, where fluorescent streptavidin was omitted.
1024 After incubation at 4°C for 30 min, the samples were centrifuged and resuspended in HBSS. Flow
1025 cytometry was used to determine the percentage of biotinylated erythrocytes.

1026 **Preparation of Stressed RBCs for Erythrophagocytosis Assays**

1027 The preparation and staining of stressed RBCs followed a previously outlined procedure[27,39]. To
1028 obtain the RBCs, mice were humanely euthanized, and whole blood was aseptically collected via
1029 cardiac puncture into CPDA-1 solution (Sigma-Aldrich, C4431) with a final concentration of 10%.
1030 The collected whole blood was combined, and plasma was separated by centrifugation at 400 g for
1031 15 min at 4°C, then filtered through a 0.1 μm filter and stored at 4°C. The RBCs were then
1032 suspended in HBSS, and leukocytes were eliminated using Lymphosep (Biowest, L0560-500).
1033 Following this, the cells were subjected to a 30-minute heating period at 48°C with continuous
1034 agitation to generate stressed RBCs. To stain the sRBCs, 1×10^{10} RBCs were resuspended in 1 ml
1035 of diluent C and mixed with 1 ml of diluent C containing 4 μM of PKH-67 (Sigma-Aldrich,
1036 MINI67) or PKH-26 (Sigma-Aldrich, MINI26). The mixture was then incubated in the dark for 5
1037 min at 37°C, and the reaction was stopped by adding 10 mL of HBSS containing 2% FCS and 0.5%
1038 BSA. Staining was followed by two washing steps with HBSS. For *in vitro* EP assays, the cells
1039 were resuspended in RPMI-1640 and counted. For the *in vivo* approach, RBCs were resuspended
1040 to 50% hematocrit in previously collected and filtered plasma.

1041 ***In Vitro* Erythrophagocytosis**

1042 On the 8th day post-seeding, stained, and counted sRBCs were added to iRPMs on 12-well plates
1043 in 10-fold excess for 1.5 h at 37 °C and 5% CO_2. After incubation, the cells were extensively
1044 washed with cold HBSS to eliminate any non-engulfed sRBCs. Subsequently, the cells were
1045 detached using Accutase (BioLegend, 423201), which were then transferred to a round-bottom
1046 FACS tube, washed with HBSS, and centrifuged at 600 g for 5 min. The cells were labeled with
1047 antibodies and analyzed using flow cytometry. For time-lapse confocal imaging of the execution
1048 of RBC uptake by iRPMs, sRBCs were stained with pH-sensitive pHrodo™ Deep Red Mammalian
1049 and Bacterial Cell Labeling Kit. The imaging was performed using the Opera Phenix

1050 (PerkinElmer), an automated confocal spinning disk microscope. Imaging was conducted for 120
1051 min, with acquisition every 1.3 min.

1052 ***In Vivo* Erythrophagocytosis**

1053 The mice were intravenously transfused with 100 µL of RBCs resuspended in plasma to 50%
1054 hematocrit. The animals were kept in cages with ad libitum access to food and water for 1.5 h
1055 before being sacrificed for organ isolation.

1056 **Mini-Hepcidin (PR73) Preparation**

1057 An optimized protocol was developed for preparing mini-Hepcidin (PR73, a kind gift from
1058 Elizabeta Nemeth, UCLA, USA) for intraperitoneal injection in mice. Commercially available
1059 PR73 powder may not represent the pure peptide, so we adjusted the preparation based on the
1060 estimated active component content (80%). The process began by precisely weighing the PR73
1061 powder to account for the estimated 80% active component. This powder was then dissolved in
1062 80% ethanol to ensure complete extraction of the peptide. The solution was thoroughly mixed using
1063 a vortex mixer to achieve a homogenous suspension. Next, the solution was carefully transferred
1064 to a sterile, low-bind vial (SL-220) to minimize potential losses due to adsorption during
1065 incubation. A brief heat treatment at 37°C for a few seconds facilitated the complete dissolution of
1066 any undissolved particles. Following the heat treatment, the vial cap was removed, and the solution
1067 was aliquoted into designated culture tubes for individual injections. A Speedvac concentrator was
1068 then used to evaporate the ethanol, resulting in a concentrated PR73 gel within each tube. To
1069 achieve a final working concentration of 0.5 nmol/µl, 2 ml of sterile, injectable-grade water was
1070 added to each tube containing the PR73 gel. The tubes were vigorously vortexed to ensure complete
1071 dissolution of the gel and homogenization of the solution. For *in vivo* experiments, 100 µl of the
1072 prepared PR73 stock solution was administered per mouse via intraperitoneal injection. A solvent
1073 control solution was prepared by following the same steps outlined above but substituting the PR73
1074 solution with only 80% ethanol. This control solution served as a baseline for comparison with the
1075 PR73-treated mice in subsequent experiments.

1076 **Live-Cell Imaging of Erythrophagocytosis in iRPMs**

1077 To assess erythrophagocytic capacity, iRPMs were seeded in Greiner Bio-One CELLSTAR
1078 µClear™ 96-well, Cell Culture-Treated, Flat-Bottom Microplate and cultured with IB versus ID
1079 serum. iRPMs with ID serum were treated with PR73 for 4 h. Following PR73 treatment, iRPMs
1080 were exposed to temperature-stressed, pHrodo-labeled RBCs, prepared using the pHrodo™ Deep

1081 Red Mammalian and Bacterial Cell Labeling Kit (Thermo Fisher Scientific). The stressed and
1082 labeled RBCs were added to the wells, and the plate was immediately transferred to the Opera
1083 Phenix™ High-Content Screening System (PerkinElmer), maintained at 37°C with 5% CO_2. Live-
1084 cell imaging was performed for 2 h with images captured at regular intervals to monitor the uptake
1085 of RBCs, and data were analyzed using Harmony High-Content Imaging and Analysis Software
1086 (PerkinElmer).

1087 **BCAA levels**

1088 Intracellular branched-chain amino acid content was quantified in magnetically sorted $CD3^+$ T
1089 cells, $B220^+$ B cells, together with $GR1^+$ granulocytes, RPMs, peritoneal macrophages, and Kupffer
1090 cells, using the Branched Chain Amino Acid Assay Kit (Sigma-Aldrich, MAK003) following the
1091 manufacturer's instructions.

1092 **Metabolic Flux Seahorse Assay**

1093 Metabolic flux was assessed using a Seahorse XF-96 Extracellular Flux Analyzer (Agilent
1094 Technologies) Mito Stress Test (Agilent,103010-100). Magnetically sorted RPMs (8×10^4
1095 cells/well) from IB and ID mice were plated onto poly-L-lysine-coated Seahorse XF HS Miniplates
1096 (Agilent, 103725-100). Cells were incubated in Seahorse XF RPMI medium (Agilent, 103576-100)
1097 supplemented with 2 mM L-glutamine (Agilent, 103579-100), 1 mM sodium pyruvate (Agilent,
1098 103578-100), and 25 mM glucose (pH adjusted to 7.4; Agilent 103577-100) at 37°C in a non-CO_2
1099 incubator for 60 min. Real-time oxygen consumption rate (OCR) was measured under basal
1100 conditions and following sequential injections of 1 μM oligomycin, 1 μM FCCP, and a mixture of
1101 1 μM rotenone and 1 μM antimycin A.

1102 **Mitochondrial substrate utilization (MitoPlate) Assay**

1103 Mitochondrial substrate utilization was assessed using the MitoPlate S-1 assay (Biolog, 14105)
1104 according to the manufacturer's protocol. Magnetically sorted RPMs from IB, ID, and ID+ERG240
1105 mice were pooled (four mice per condition), counted, and resuspended in MitoPlate assay medium
1106 before seeding at 8×10^4 cells per well onto the precoated 96-well Mitoplates, containing the dye
1107 mix MC. Plates were loaded into a Tecan Infinite 200 Pro maintained at 37°C, and kinetic OD_{590}
1108 measurements were collected every 10 min throughout the assay. Absolute blank-corrected OD
1109 values from the 6-h time point were used for analysis.

1110

1111

1112 **Voluntary Oral Drug Administration**

1113 Strawberry-flavored gelatin jellies were prepared under sterile conditions in 96-well plates (100
1114 μL/well), with or without ENTO and ERG240. Gelatin (8% w/v, Sigma-Aldrich, G9391) was
1115 dissolved in warm, sterile water, and strawberry flavoring essence (1% v/v, OstroVit,
1116 5903933916217) was added. Just before gelation, ENTO or ERG240 was added to the appropriate
1117 wells of a sterile 96-well plate to achieve the desired final concentration, while control wells
1118 received vehicle only. The gelatin solution (100 μL) was then added to each well, and the plates
1119 were refrigerated at 4°C until solid. To acclimate IB and ID mice, two drug-free jellies were
1120 provided per cage daily for 2-3 days (two mice per cage). This co-housing approach minimized
1121 stress associated with individual training. Following acclimation, mice readily consumed the jellies
1122 within 15-20 min. Drug-containing jellies were administered at approximately the same time each
1123 day for two or three weeks.

1124 **Generation of Ferroportin Overexpressing iRPMs**

1125 We successfully cloned the wild-type *Slc40a1* gene, encoding mouse ferroportin (FPN; Uniport
1126 ID: Q9JHI9), into the HIV SFFV lentiviral vector. Lentiviral production involved transfecting the
1127 chosen lentiviral vectors (FPN or Mock) along with the psPAX2 packaging vector and the pMD2.G
1128 envelope vector into HEK293T cells. The resulting viral supernatants were harvested and titrated
1129 to determine viral concentration. Subsequently, iRPMs were transduced on Day 1 with lentiviral
1130 vectors at a multiplicity of infection (MOI) of 1. On Days 4 and 6, the culture medium was replaced
1131 with fresh complete medium supplemented with 20 μM hemin. Expression levels of surface FPN
1132 were measured in each experiment using flow cytometry. This verification step confirmed
1133 successful FPN overexpression in iRPM population, allowing for functional analysis of the
1134 consequences in subsequent experiments.

1135 **Hepcidin Measurement with ELISA**

1136 Serum hepcidin levels were measured using the Hepcidin-Murine Compete ELISA Kit (Intrinsic
1137 LifeSciences, HMC-001) following the manufacturer's instructions. Optical density was
1138 determined with a microplate reader at a wavelength of 450 nm.

1139 **Erythropoietin (EPO) Measurement with ELISA**

1140 Serum EPO levels were measured using the Mouse Erythropoietin/EPO Quantikine ELISA Kit
1141 (R&D Systems, MEP00B) following the manufacturer's instructions. Optical density was
1142 determined with a microplate reader at a wavelength of 450 nm.

1143 **Transferrin Saturation and Tissue Iron Measurements**

1144 The levels of serum iron and unsaturated iron-binding capacity were quantified using SFBC
1145 (Biolabo, 80008) and UIBC (Biolabo, 97408) kits per the manufacturer's instructions. Transferrin
1146 saturation was determined using the formula SFBC/(SFBC+UIBC) x 100. Tissue non-heme iron
1147 content was measured using the bathophenanthroline method, and the results were calculated based
1148 on tissue dry weight, as previously described[89].

1149 **RT-qPCR**

1150 RNA from cell pellets was isolated using an RNA purification kit (Eurex) according to the
1151 manufacturer's instructions. RNA from liver, heart and kidney tissues was isolated using TRIzol™
1152 reagent according to the manufacturer's instructions. 400 ng of RNA was subjected to reverse
1153 transcription. In the first stage of the reaction, RNA was denatured, and random primers were
1154 attached. For this purpose, a mixture consisting of 400 ng RNA, 1 µL of random primers at a
1155 concentration of 200 ng/µL, and nuclease-free water was prepared so that the total reaction volume
1156 was 17.7 µL. The mixture was incubated at 70°C for 10 min and then cooled to 4°C. The next step
1157 was to add the reaction mixture to the tubes, which contained: 0.3 µl RevertAid H Minus reverse
1158 transcriptase, 1 µL of 10 mM dNTP solution, and 5 µL of reaction buffer. The total reaction volume
1159 was 25 µL. The reaction was carried out for 60 min at 42°C, 70°C, 10 min. The obtained cDNA
1160 was diluted 9x and then used for quantitative polymerase chain reaction (qPCR). The reaction
1161 mixture consisted of 4 µL cDNA, 7.5 µL SG qPCR Master Mix (2x), and 1.5 µL of a 5 µM solution
1162 of forward and reverse primers. The whole was supplemented with nuclease-free water to a final
1163 reaction volume of 15 µL. The qPCR reaction was carried out using the LightCycler 96 Real-Time
1164 PCR System (Roche). The reaction was pre-incubated at 95°C for 600 s, and then two-step
1165 amplification was performed 40x (95°C x 15 s, 60°C x 60 s).

1166 **Immunohistochemistry of Spleen Tissues**

1167 The spleen was fixed in 4% PFA at 4°C for 24 h. Tissues were washed with PBS (3x30min) and
1168 incubated for 2 h in 12.5% and then in 25% sucrose solution for 48 h. Subsequently, spleen tissue
1169 fragments were embedded in the Cryomatrix medium, frozen in liquid nitrogen, and cut into 10 µm
1170 thick sections using a cryo microtome (Leica). The sections were mounted on glass slides and
1171 stored at -20°C. Before staining, the sections were warmed at room temperature for 30 min, and
1172 then their edges were surrounded using a Pap Pen Liquid Blocker. Next, the slides with sections
1173 were washed in PBS for 10 min and permeabilized in 0.1% Triton X-100 solution for 20 min.

1174 Nonspecific antibody binding was blocked by incubating the sections in 3% BSA solution for 1 h
1175 at room temperature. To visualize RPMs, the tissues were incubated with FITC-conjugated F4/80
1176 antibody (1:100), and for FPN, with Alexa Fluor 647-conjugated FPN antibody (1:100) in 3% BSA
1177 for 2 h at room temperature in the dark. After incubation with antibodies, the tissues were washed
1178 5 x 5 min in 0.1% Triton X-100 solution to remove unbound antibodies. To stain cell nuclei, the
1179 sections were incubated with Hoechst 33342 diluted in 0.1% Triton X-100 solution (final
1180 concentration 1 μg/ml) for 10 min at room temperature in the dark. Then, the sections were washed
1181 for 3 x 5 min in 0.1% Triton X-100 solution, incubated in PBS for 10 min, and mounted with a
1182 coverslip using ProLong™ Glass Antifade Mountant. Samples were imaged on a confocal
1183 microscope with a Plan-Apochromat 40x/1.3 NA oil immersion objective (Zeiss) LSM 800.

1184 **Histological and Histochemical Analysis**

1185 Following fixation in 10% formalin for 24 h, spleens were stored in 70% ethanol before further
1186 preparation. The tissue was embedded in paraffin and 7 μm cross-sections were cut with a
1187 microtome (Reichert-Jung, Germany). Sections were prepared as described above. After mounting
1188 on glass slides, sections were deparaffinized, incubated with a working solution containing Perls'
1189 Prussian Blue for 30 min, counterstained with pararosaniline solution for 2 min, and analyzed under
1190 standard light microscopy (Olympus CH2).

1191 **Transcriptome analysis by RNA-seq**

1192 RNA-seq libraries were generated from FACS-sorted RPMs (minimum 100,000 cells per sample)
1193 using the Smart-seq2 protocol[90], which is optimized for low-input total mRNA sequencing. RNA
1194 integrity and library quality were checked by a Bioanalyzer. Sequencing was performed on an
1195 Illumina NextSeq500 platform, producing 75-bp single-end reads at ~50 million reads per sample.
1196 RNA-seq was carried out at the EMBL GeneCore facility (Heidelberg, Germany). Sequence reads
1197 were trimmed to remove possible adapter sequences and nucleotides with poor quality using
1198 Trimmomatic v.0.36. The trimmed reads were mapped to the Mus musculus GRCm38 reference
1199 genome available on ENSEMBL using the STAR aligner v.2.5.2b. Unique gene hit counts were
1200 calculated by using featureCounts from the Subread package v.1.5.2. Normalization and differential
1201 expression analysis were performed using DESeq2. The Wald test was used to generate p-values
1202 and log2 fold changes. Genes with an adjusted p-value < 0.05 and absolute log2 fold change > 1
1203 were called as differentially expressed genes.

1204

1205 **Proteomic analysis of RPMs**

1206 Sample Preparation. Magnetically isolated RPMs were obtained from the spleens of IB and ID
1207 female C57BL/6J mice. The cells were lysed using RIPA buffer. Proteins were precipitated using a
1208 chloroform/methanol method, washed with methanol, and reconstituted in 100 mM HEPES (pH
1209 8.0) containing 10 mM TCEP and 10 mM chloroacetamide.

1210 LC-MS/MS Analysis. 10 µg of each lysate was subjected to an in-solution tryptic digest using a
1211 modified version of the Single-Pot Solid-Phase-enhanced Sample Preparation (SP3) protocol[91,92].
1212 To this end, lysates were added to Sera-Mag Beads (Thermo Scientific, #4515-2105-050250, 6515-
1213 2105-050250) in 10 µl 15% formic acid and 30 µl of ethanol. The binding of proteins was achieved
1214 by shaking for 15 min at room temperature. SDS was removed by 4 subsequent washes with 200
1215 µl of 70% ethanol. Proteins were digested overnight at room temperature with 0.4 µg of sequencing
1216 grade modified trypsin (Promega, V5111) in 40 µl Hepes/NaOH, pH 8.4 in the presence of 1.25
1217 mM TCEP and 5 mM chloroacetamide (Sigma-Aldrich, C0267). Beads were separated and washed
1218 with 10 µl of an aqueous solution of 2% DMSO, and the combined eluates were dried down.

1219 Up to 10 µg of peptides per sample were labeled with TMT10plex™ reagents following established
1220 protocols[93]. Briefly, 0.8 mg of TMT reagent was dissolved in 45 µL of anhydrous acetonitrile, and
1221 4 µL of this solution was added to each peptide sample. Labeling was carried out at room
1222 temperature for 1 h. The reaction was quenched by adding 4 µL of 5% hydroxylamine in water,
1223 followed by a 15-minute incubation at room temperature. Labeled peptides were pooled for
1224 multiplexing, desalted using an Oasis® HLB µElution Plate (Waters #186001828BA) according to
1225 the manufacturer's instructions, and dried by vacuum centrifugation.

1226 Offline high-pH reversed-phase fractionation was performed as described previously[94], using an
1227 Agilent 1200 Infinity HPLC system equipped with a Gemini C18 analytical column (3 µm particle
1228 size, 110 Å pore size, 100 × 1.0 mm; Phenomenex) and a matching Gemini C18 SecurityGuard pre-
1229 column (4 × 2.0 mm; Phenomenex). Peptides were separated at a flow rate of 0.1 mL/min using
1230 mobile phase A (20 mM ammonium formate, pH 10.0) and mobile phase B (100% acetonitrile).
1231 The chromatographic gradient was as follows: 100% A for 2 min, linear increase to 35% B over
1232 59 min, ramp to 85% B in 1 min, held at 85% B for 15 min, followed by re-equilibration at 100%
1233 A for 13 min. A total of 48 fractions were collected and subsequently pooled into 12 final fractions.
1234 Nanoflow LC-MS/MS analysis was performed on an UltiMate 3000 RSLCnano system (Thermo
1235 Fisher Scientific) coupled to an Orbitrap Fusion™ Lumos™ Tribrid™ mass spectrometer (Thermo

1236 Fisher Scientific). Peptides were initially loaded onto a µ-Precolumn C18 PepMap™ 100 trap
1237 cartridge (300 µm i.d. × 5 mm, 5 µm particles, 100 Å; Thermo) at 30 µL/min with 0.05% TFA in
1238 water for 6 min. Analytical separation was carried out using a nanoEase™ M/Z HSS T3 column
1239 (75 µm i.d. × 250 mm, 1.8 µm particles, 100 Å; Waters), equilibrated with solvent A (3% DMSO,
1240 0.1% formic acid in water). Peptides were eluted at 0.3 µL/min using a gradient of solvent B (3%
1241 DMSO, 0.1% formic acid in acetonitrile) as follows: 2–8% B over 6 min, 8–25% over 99 min, 25–
1242 40% over 5 min, ramp to 85% in 0.1 min, held at 85% for 3.9 min, followed by re-equilibration to
1243 2% B for 6 min. Mass spectrometry was performed using a Pico-Tip emitter (360 µm OD × 20 µm
1244 ID, 10 µm tip; CoAnn Technologies) with a spray voltage of 2.4 kV and a capillary temperature of
1245 275 °C. Full MS scans were acquired in the Orbitrap at a resolution of 120,000 (at m/z 200), over
1246 a mass range of m/z 375–1,500, with an AGC target set to 'standard' and a maximum injection time
1247 of 50 ms. The instrument operated in data-dependent acquisition (DDA) mode. MS/MS spectra
1248 were acquired in the Orbitrap at a resolution of 30,000, with a maximum injection time of 94 ms
1249 and an AGC target of 200%. Precursors were fragmented using higher-energy collisional
1250 dissociation (HCD) at 36% normalized collision energy. A quadrupole isolation window of 0.7 m/z
1251 was used, with dynamic exclusion set to 60 s. Only precursor ions with charge states between 2
1252 and 7 were selected for fragmentation.

1253 Acquired data were analyzed using IsobarQuant and Mascot V2.4 (Matrix Science) using a reverse
1254 UniProt FASTA Mus musculus database (UP000000589), including common contaminants. The
1255 following modifications were considered: Carbamidomethyl (C, fixed), TMT10plex (K, fixed),
1256 Acetyl (N-term, variable), Oxidation (M, variable), and TMT10plex (N-term, variable). The mass
1257 error tolerance for full scan MS spectra was set to 10 ppm, and for MS/MS spectra to 0.02 Da. A
1258 maximum of 2 missed cleavages were allowed. A minimum of 2 unique peptides with a peptide
1259 length of at least seven amino acids and a false discovery rate below 0.01 were required on the
1260 peptide and protein level.

1261 Data Processing. The data were processed using MaxQuant 2.1.3.0, with peptides identified from
1262 MS/MS spectra searched against the Uniprot Mouse Reference Proteome (UP000000589) using
1263 the built-in Andromeda search engine. Fixed modifications included cysteine
1264 carbamidomethylation, while variable modifications included methionine oxidation,
1265 glutamine/asparagine deamination, and protein N-terminal acetylation. In silico digests allowed for
1266 cleavages of arginine or lysine followed by any amino acid (trypsin/P), with up to two missed
1267 cleavages permitted. The false discovery rate (FDR) was set to 0.01 for peptides, proteins, and

1268 sites. Match between runs was enabled, and other parameters were used as preset in the software.
1269 Protein identification and intrasample quantification were performed using the iBAQ algorithm in
1270 MaxQuant.

1271 **Transmission Electron Microscopy (TEM) of the Spleen**

1272 Fresh spleen samples, approximately 3 mm^2 in size, were fixed in 2.5% glutaraldehyde for 24 h at
1273 4°C. Following fixation, the samples were washed in PBS and postfixed with 1% osmium tetroxide
1274 for 1 h. After rinsing with water, the samples were incubated in 1% aqueous uranyl acetate for 12
1275 h at 4°C. The samples were then dehydrated at room temperature using increasing concentrations
1276 of ethanol, infiltrated with epoxy resin (Sigma-Aldrich, 45-359-1EA-F), and polymerized for 48 h
1277 at 60°C. The polymerized resin blocks were trimmed using a tissue processor (Leica EM TP) and
1278 sectioned into ultrathin slices (65 nm thick) with an ultramicrotome (EM UC7, Leica). These
1279 ultrathin sections were collected on nickel grids with 200 mesh (Agar Scientific, G2200N). The
1280 specimen grids were examined with a Tecnai T12 BioTwin transmission electron microscope (FEI,
1281 Hillsboro, OR, USA) equipped with a 16-megapixel TemCam-F416 camera (TVIPS GmbH) at the
1282 in-house Microscopy and Cytometry Facility.

1283 **Preparation of Schematic Figures**

1284 The graphical abstract was created in BioRender. Mleczko-Sanecka, K. (2025)
1285 https://BioRender.com/y54j6da.

1286 **Statistical Analysis**

1287 Female mice of the same age were randomly assigned to experimental groups. Samples derived
1288 from mice were collected and assessed/measured randomly, and harvested in a different order
1289 across individual experiments. The sample size, typically ranging from 5 to 9 mice per group or
1290 independent biological cell-based experiments, was determined based on power analysis, prior
1291 experience with similar experiments, and previously published studies in the field of RPM biology.
1292 Statistical analysis was conducted using GraphPad Prism (GraphPad Software, Version 9). Data
1293 are presented as mean ± SEM unless otherwise noted. Student's t-test with Welch's correction was
1294 employed when comparing the two groups. For comparisons involving more than two groups, one-
1295 way ANOVA was used, or two-way ANOVA when the simultaneous effects of two factors were
1296 being evaluated. Tukey's test was implemented for post-hoc analysis following ANOVA. The
1297 following notation was used to indicate statistically significant differences between means: ns for

non-significant ($p > 0.05$), * for $p < 0.05$, ** for $p < 0.01$, *** for $p < 0.001$, and **** for $p < 0.0001$.

Data availability

Mass spectrometry proteomics data were deposited to the ProteomeXchange Consortium via the PRIDE partner repository with the dataset identifiers: Project accession: PXD064719 (access secured by a token: lKilHQArXhhB). RNA sequencing data are available in Gene Expression Omnibus GEO under the accession number GSE312948, and metadata were deposited to SRA (PRJNA1274426).

Authorship Contributions

KMS, PKM, RM, KC and PS conceived and planned the experiments; PKM, RM, KC, PS, GZ, MN, AJ, and ML performed research; PKM, RM, KC, PS, GZ, KMS and ML analyzed and visualized data; EN, ZL and FG provided critical reagents/models, KC and KMS curated data; KMS, WP, and EN supervised the study; KC edited the manuscript; PKM, RM and KMS wrote the manuscript.

Conflict of interest

EN is a shareholder and scientific advisor of Intrinsic LifeSciences and Silarus Therapeutics, and a consultant for Disc Medicine, Ionis Pharmaceuticals, Protagonist, GSK and Vifor. Other authors have declared that no conflict of interest exists.

Acknowledgments

We thank the EMBL Proteomics Core Facility (EMBL, Heidelberg) for performing RPM proteomic profiling and data analysis, and the GeneCore team (EMBL, Heidelberg) for performing RNA sequencing. We thank Tara Arvedson (Amgen Inc., USA) for the anti-ferroportin antibody, Elizabeta Nemeth (UCLA, USA) for PR73, Florent Ginhoux for access to Ms4a3-Cre mice, and Aneta Suwińska for sharing UBI-GFP/BL6 mice, and Vania Manolova (CSL Vifor) for providing vamifeport. Many thanks to Agnieszka Popielska and Anna Kosson, and the staff of the Experimental Medicine Centre (Bialystok, Poland) and Mossakowski Medical Research Institute (Warsaw, Poland) for their technical support. We thank Sylwia Herman for her assistance with the histological analyses and Enrico Tatti for consulting on the MitoPlates profiling data. Mouse-based experiments and animal housing were supported by the Rodent Facility, EM, and Opera Phenix imaging were performed at the Microscopy Facility, and lentiviral DNA constructs were generated

at the Genome Engineering Facility of IIMCB (IN-MOL-CELL Infrastructure) funded by the European Union – NextGenerationEU under the National Recovery and Resilience Plan. IN-MOL-CELL Infrastructure was also funded by the European Union under Horizon Europe (Project 101059801 - RACE) and by the RACE-PRIME project carried out within the IRAP programme of the Foundation for Polish Science, co-financed by the European Union under the European Funds for Smart Economy 2021-2027 (FENG). Pratik Kumar Mandal gratefully acknowledges funding from the National Science Centre PRELUDIUM 22 grant, which supported experiments involving lentiviral-mediated FPN overexpression (UMO-2023/49/N/NZ3/04232). This work was funded by the National Science Centre Sonata Bis grant (UMO-2020/38/E/NZ4/00511).

During the preparation of this work, the authors used ChatGPT 5.2 to assist with language editing in a limited number of instances. After using this tool, the authors reviewed and edited the content as needed and take full responsibility for the content of the published article.

References

1. Boada-Romero, E., Martinez, J., Heckmann, B.L., and Green, D.R. (2020). The clearance of dead cells by efferocytosis. Nat Rev Mol Cell Biol *21*, 398–414. https://doi.org/10.1038/s41580-020-0232-1.

2. Doran, A.C., Yurdagul, A., and Tabas, I. (2020). Efferocytosis in health and disease. Nat Rev Immunol *20*, 254–267. https://doi.org/10.1038/s41577-019-0240-6.

3. Moon, B., Yang, S., Moon, H., Lee, J., and Park, D. (2023). After cell death: the molecular machinery of efferocytosis. Exp Mol Med *55*, 1644–1651. https://doi.org/10.1038/s12276-023-01070-5.

4. Sheng, Y.R., Hu, W.T., Chen, S., and Zhu, X.Y. (2024). Efferocytosis by macrophages in physiological and pathological conditions: regulatory pathways and molecular mechanisms. Front Immunol *15*, 1275203. https://doi.org/10.3389/fimmu.2024.1275203.

5. Schilperoort, M., Ngai, D., Sukka, S.R., Avrampou, K., Shi, H., and Tabas, I. (2023). The role of efferocytosis-fueled macrophage metabolism in the resolution of inflammation. Immunol Rev *319*, 65–80. https://doi.org/10.1111/imr.13214.

6. Mukundan, L., Odegaard, J.I., Morel, C.R., Heredia, J.E., Mwangi, J.W., Ricardo-Gonzalez, R.R., Goh, Y.P.S., Eagle, A.R., Dunn, S.E., Awakuni, J.U.H., et al. (2009). PPAR-delta senses and orchestrates clearance of apoptotic cells to promote tolerance. Nat Med *15*, 1266–1272. https://doi.org/10.1038/nm.2048.

7. A-Gonzalez, N., Bensinger, S.J., Hong, C., Beceiro, S., Bradley, M.N., Zelcer, N., Deniz, J., Ramirez, C., Díaz, M., Gallardo, G., et al. (2009). Apoptotic cells promote their own clearance and immune tolerance through activation of the nuclear receptor LXR. Immunity *31*, 245–258. https://doi.org/10.1016/j.immuni.2009.06.018.

8. Mota, A.C., Dominguez, M., Weigert, A., Snodgrass, R.G., Namgaladze, D., and Brüne, B. (2021). Lysosome-Dependent LXR and PPARδ Activation Upon Efferocytosis in Human Macrophages. Front Immunol *12*, 637778. https://doi.org/10.3389/fimmu.2021.637778.

9. Schilperoort, M., Ngai, D., Katerelos, M., Power, D.A., and Tabas, I. (2023). PFKFB2-mediated glycolysis promotes lactate-driven continual efferocytosis by macrophages. Nat Metab *5*, 431–444. https://doi.org/10.1038/s42255-023-00736-8.

10. Morioka, S., Perry, J.S.A., Raymond, M.H., Medina, C.B., Zhu, Y., Zhao, L., Serbulea, V., Onengut-Gumuscu, S., Leitinger, N., Kucenas, S., et al. (2018). Efferocytosis induces a novel SLC program to promote glucose uptake and lactate release. Nature *563*, 714–718. https://doi.org/10.1038/s41586-018-0735-5.

11. Zhang, S., Weinberg, S., DeBerge, M., Gainullina, A., Schipma, M., Kinchen, J.M., Ben-Sahra, I., Gius, D.R., Yvan-Charvet, L., Chandel, N.S., et al. (2019). Efferocytosis Fuels Requirements of Fatty Acid Oxidation and the Electron Transport Chain to Polarize Macrophages for Tissue Repair. Cell Metab *29*, 443-456.e5. https://doi.org/10.1016/j.cmet.2018.12.004.

12. Wang, Y., Subramanian, M., Yurdagul, A., Barbosa-Lorenzi, V.C., Cai, B., de Juan-Sanz, J., Ryan, T.A., Nomura, M., Maxfield, F.R., and Tabas, I. (2017). Mitochondrial Fission Promotes the Continued Clearance of Apoptotic Cells by Macrophages. Cell *171*, 331-345.e22. https://doi.org/10.1016/j.cell.2017.08.041.

13. Jiang, S., Park, D.W., Stigler, W.S., Creighton, J., Ravi, S., Darley-Usmar, V., and Zmijewski, J.W. (2013). Mitochondria and AMP-activated protein kinase-dependent mechanism of efferocytosis. J Biol Chem *288*, 26013–26026. https://doi.org/10.1074/jbc.M113.489468.

14. Tsai, T.-L., Zhou, T.-A., Hsieh, Y.-T., Wang, J.-C., Cheng, H.-K., Huang, C.-H., Tsai, P.-Y., Fan, H.-H., Feng, H.-K., Huang, Y.-C., et al. (2022). Multiomics reveal the central role of pentose phosphate pathway in resident thymic macrophages to cope with efferocytosis-associated stress. Cell Rep *40*, 111065. https://doi.org/10.1016/j.celrep.2022.111065.

15. He, D., Mao, Q., Jia, J., Wang, Z., Liu, Y., Liu, T., Luo, B., and Zhang, Z. (2021). Pentose Phosphate Pathway Regulates Tolerogenic Apoptotic Cell Clearance and Immune Tolerance. Front Immunol *12*, 797091. https://doi.org/10.3389/fimmu.2021.797091.

16. Yurdagul, A., Subramanian, M., Wang, X., Crown, S.B., Ilkayeva, O.R., Darville, L., Kolluru, G.K., Rymond, C.C., Gerlach, B.D., Zheng, Z., et al. (2020). Macrophage Metabolism of Apoptotic Cell-Derived Arginine Promotes Continual Efferocytosis and Resolution of Injury. Cell Metab *31*, 518-533.e10. https://doi.org/10.1016/j.cmet.2020.01.001.

17. Ampomah, P.B., Cai, B., Sukka, S.R., Gerlach, B.D., Yurdagul, A., Wang, X., Kuriakose, G., Darville, L.N.F., Sun, Y., Sidoli, S., et al. (2022). Macrophages use apoptotic cell-derived

1399 methionine and DNMT3A during efferocytosis to promote tissue resolution. Nat Metab *4*, 444–
1400 457. https://doi.org/10.1038/s42255-022-00551-7.

1401 18. Sukka, S.R., Ampomah, P.B., Darville, L.N.F., Ngai, D., Wang, X., Kuriakose, G., Xiao, Y.,
1402 Shi, J., Koomen, J.M., McCusker, R.H., et al. (2024). Efferocytosis drives a tryptophan
1403 metabolism pathway in macrophages to promote tissue resolution. Nat Metab *6*, 1736–1755.
1404 https://doi.org/10.1038/s42255-024-01115-7.

1405 19. Merlin, J., Ivanov, S., Dumont, A., Sergushichev, A., Gall, J., Stunault, M., Ayrault, M.,
1406 Vaillant, N., Castiglione, A., Swain, A., et al. (2021). Non-canonical glutamine transamination
1407 sustains efferocytosis by coupling redox buffering to oxidative phosphorylation. Nat Metab *3*,
1408 1313–1326. https://doi.org/10.1038/s42255-021-00471-y.

1409 20. Muckenthaler, M.U., Rivella, S., Hentze, M.W., and Galy, B. (2017). A Red Carpet for Iron
1410 Metabolism. Cell *168*, 344–361. https://doi.org/10.1016/j.cell.2016.12.034.

1411 21. Slusarczyk, P., and Mleczko-Sanecka, K. (2021). The Multiple Facets of Iron Recycling. Genes
1412 (Basel) *12*, 1364. https://doi.org/10.3390/genes12091364.

1413 22. Klei, T.R.L., Meinderts, S.M., van den Berg, T.K., and van Bruggen, R. (2017). From the
1414 Cradle to the Grave: The Role of Macrophages in Erythropoiesis and Erythrophagocytosis.
1415 Front Immunol *8*, 73. https://doi.org/10.3389/fimmu.2017.00073.

1416 23. Nemeth, E., Tuttle, M.S., Powelson, J., Vaughn, M.B., Donovan, A., Ward, D.M., Ganz, T., and
1417 Kaplan, J. (2004). Hepcidin regulates cellular iron efflux by binding to ferroportin and inducing
1418 its internalization. Science *306*, 2090–2093. https://doi.org/10.1126/science.1104742.

1419 24. Aschemeyer, S., Qiao, B., Stefanova, D., Valore, E.V., Sek, A.C., Ruwe, T.A., Vieth, K.R.,
1420 Jung, G., Casu, C., Rivella, S., et al. (2018). Structure-function analysis of ferroportin defines
1421 the binding site and an alternative mechanism of action of hepcidin. Blood *131*, 899–910.
1422 https://doi.org/10.1182/blood-2017-05-786590.

1423 25. Mleczko-Sanecka, K., and Silvestri, L. (2021). Cell-type-specific insights into iron regulatory
1424 processes. Am J Hematol *96*, 110–127. https://doi.org/10.1002/ajh.26001.

1425 26. Kohyama, M., Ise, W., Edelson, B.T., Wilker, P.R., Hildner, K., Mejia, C., Frazier, W.A.,
1426 Murphy, T.L., and Murphy, K.M. (2009). Role for Spi-C in the development of red pulp
1427 macrophages and splenic iron homeostasis. Nature *457*, 318–321.
1428 https://doi.org/10.1038/nature07472.

1429 27. Slusarczyk, P., Mandal, P.K., Zurawska, G., Niklewicz, M., Chouhan, K., Mahadeva, R.,
1430 Jończy, A., Macias, M., Szybinska, A., Cybulska-Lubak, M., et al. (2023). Impaired iron
1431 recycling from erythrocytes is an early hallmark of aging. Elife *12*, e79196.
1432 https://doi.org/10.7554/eLife.79196.

1433 28. Okreglicka, K., Iten, I., Pohlmeier, L., Onder, L., Feng, Q., Kurrer, M., Ludewig, B., Nielsen,
1434 P., Schneider, C., and Kopf, M. (2021). PPARγ is essential for the development of bone marrow
1435 erythroblastic island macrophages and splenic red pulp macrophages. J Exp Med *218*,
1436 e20191314. https://doi.org/10.1084/jem.20191314.

29. Delaby, C., Pilard, N., Puy, H., and Canonne-Hergaux, F. (2008). Sequential regulation of ferroportin expression after erythrophagocytosis in murine macrophages: early mRNA induction by haem, followed by iron-dependent protein expression. Biochem J *411*, 123–131. https://doi.org/10.1042/BJ20071474.

30. Bian, Z., Shi, L., Guo, Y.-L., Lv, Z., Tang, C., Niu, S., Tremblay, A., Venkataramani, M., Culpepper, C., Li, L., et al. (2016). Cd47-Sirpα interaction and IL-10 constrain inflammation-induced macrophage phagocytosis of healthy self-cells. Proc Natl Acad Sci U S A *113*, E5434-5443. https://doi.org/10.1073/pnas.1521069113.

31. Bennett, L.F., Liao, C., Quickel, M.D., Yeoh, B.S., Vijay-Kumar, M., Hankey-Giblin, P., Prabhu, K.S., and Paulson, R.F. (2019). Inflammation induces stress erythropoiesis through heme-dependent activation of SPI-C. Sci Signal *12*, eaap7336. https://doi.org/10.1126/scisignal.aap7336.

32. Ma, S., Dubin, A.E., Zhang, Y., Mousavi, S.A.R., Wang, Y., Coombs, A., Loud, M., Andolfo, I., and Patapoutian, A. (2021). A role of PIEZO1 in iron metabolism in mice and humans. Cell *184*, 969-982.e13. https://doi.org/10.1016/j.cell.2021.01.024.

33. Camaschella, C. (2019). Iron deficiency. Blood *133*, 30–39. https://doi.org/10.1182/blood-2018-05-815944.

34. Pasricha, S.-R., Tye-Din, J., Muckenthaler, M.U., and Swinkels, D.W. (2021). Iron deficiency. Lancet *397*, 233–248. https://doi.org/10.1016/S0140-6736(20)32594-0.

35. GBD 2021 Anaemia Collaborators (2023). Prevalence, years lived with disability, and trends in anaemia burden by severity and cause, 1990-2021: findings from the Global Burden of Disease Study 2021. Lancet Haematol *10*, e713–e734. https://doi.org/10.1016/S2352-3026(23)00160-6.

36. Atkinson, S.H., Suchdev, P.S., Bode, M., Carducci, B., Cerami, C., Mwangi, M.N., Namaste, S., Winichagoon, P., Leung, S., Mutua, A.M., et al. (2025). Getting back on track to meet global anaemia reduction targets: a Lancet Haematology Commission. Lancet Haematol *12*, e717–e767. https://doi.org/10.1016/S2352-3026(25)00146-2.

37. Camaschella, C., and Girelli, D. (2020). The changing landscape of iron deficiency. Mol Aspects Med *75*, 100861. https://doi.org/10.1016/j.mam.2020.100861.

38. Al-Naseem, A., Sallam, A., Choudhury, S., and Thachil, J. (2021). Iron deficiency without anaemia: a diagnosis that matters. Clin Med (Lond) *21*, 107–113. https://doi.org/10.7861/clinmed.2020-0582.

39. Theurl, I., Hilgendorf, I., Nairz, M., Tymoszuk, P., Haschka, D., Asshoff, M., He, S., Gerhardt, L.M.S., Holderried, T.A.W., Seifert, M., et al. (2016). On-demand erythrocyte disposal and iron recycling requires transient macrophages in the liver. Nat Med *22*, 945–951. https://doi.org/10.1038/nm.4146.

40. Klei, T.R.L., Dalimot, J., Nota, B., Veldthuis, M., Mul, F.P.J., Rademakers, T., Hoogenboezem, M., Nagelkerke, S.Q., van IJcken, W.F.J., Oole, E., et al. (2020). Hemolysis in the spleen drives erythrocyte turnover. Blood *136*, 1579–1589. https://doi.org/10.1182/blood.2020005351.

41. Zurawska, G., Sas, Z., Jończy, A., Mahadeva, R., Slusarczyk, P., Chwałek, M., Seehofer, D., Damm, G., Mazgaj, R., Skórzyński, M., et al. (2026). Liver sinusoidal endothelial cells constitute a major route for hemoglobin clearance. EMBO Rep. https://doi.org/10.1038/s44319-025-00673-5.

42. Akilesh, H.M., Buechler, M.B., Duggan, J.M., Hahn, W.O., Matta, B., Sun, X., Gessay, G., Whalen, E., Mason, M., Presnell, S.R., et al. (2019). Chronic TLR7 and TLR9 signaling drives anemia via differentiation of specialized hemophagocytes. Science *363*, eaao5213. https://doi.org/10.1126/science.aao5213.

43. Liu, Z., Gu, Y., Chakarov, S., Bleriot, C., Kwok, I., Chen, X., Shin, A., Huang, W., Dress, R.J., Dutertre, C.-A., et al. (2019). Fate Mapping via Ms4a3-Expression History Traces Monocyte-Derived Cells. Cell *178*, 1509-1525.e19. https://doi.org/10.1016/j.cell.2019.08.009.

44. Palmieri, M., Impey, S., Kang, H., di Ronza, A., Pelz, C., Sardiello, M., and Ballabio, A. (2011). Characterization of the CLEAR network reveals an integrated control of cellular clearance pathways. Hum Mol Genet *20*, 3852–3866. https://doi.org/10.1093/hmg/ddr306.

45. Bussi, C., and Gutierrez, M.G. (2024). One size does not fit all: Lysosomes exist in biochemically and functionally distinct states. PLoS Biol *22*, e3002576. https://doi.org/10.1371/journal.pbio.3002576.

46. Rovira, M., Sereda, R., Pladevall-Morera, D., Ramponi, V., Marin, I., Maus, M., Madrigal-Matute, J., Díaz, A., García, F., Muñoz, J., et al. (2022). The lysosomal proteome of senescent cells contributes to the senescence secretome. Aging Cell *21*, e13707. https://doi.org/10.1111/acel.13707.

47. Vinchi, F., Costa da Silva, M., Ingoglia, G., Petrillo, S., Brinkman, N., Zuercher, A., Cerwenka, A., Tolosano, E., and Muckenthaler, M.U. (2016). Hemopexin therapy reverts heme-induced proinflammatory phenotypic switching of macrophages in a mouse model of sickle cell disease. Blood *127*, 473–486. https://doi.org/10.1182/blood-2015-08-663245.

48. Pfefferlé, M., Ingoglia, G., Schaer, C.A., Yalamanoglu, A., Buzzi, R., Dubach, I.L., Tan, G., López-Cano, E.Y., Schulthess, N., Hansen, K., et al. (2020). Hemolysis transforms liver macrophages into antiinflammatory erythrophagocytes. J Clin Invest *130*, 5576–5590. https://doi.org/10.1172/JCI137282.

49. Pereira, M., Chen, T.-D., Buang, N., Olona, A., Ko, J.-H., Prendecki, M., Costa, A.S.H., Nikitopoulou, E., Tronci, L., Pusey, C.D., et al. (2019). Acute Iron Deprivation Reprograms Human Macrophage Metabolism and Reduces Inflammation In Vivo. Cell Rep *28*, 498-511.e5. https://doi.org/10.1016/j.celrep.2019.06.039.

50. Pagani, A., Nai, A., Corna, G., Bosurgi, L., Rovere-Querini, P., Camaschella, C., and Silvestri, L. (2011). Low hepcidin accounts for the proinflammatory status associated with iron deficiency. Blood *118*, 736–746. https://doi.org/10.1182/blood-2011-02-337212.

1512 51. Diskin, C., and Pålsson-McDermott, E.M. (2018). Metabolic Modulation in Macrophage
1513 Effector Function. Front Immunol *9*, 270. https://doi.org/10.3389/fimmu.2018.00270.

1514 52. Luo, B., Gan, W., Liu, Z., Shen, Z., Wang, J., Shi, R., Liu, Y., Liu, Y., Jiang, M., Zhang, Z., et
1515 al. (2016). Erythropoeitin Signaling in Macrophages Promotes Dying Cell Clearance and
1516 Immune Tolerance. Immunity *44*, 287–302. https://doi.org/10.1016/j.immuni.2016.01.002.

1517 53. Finberg, K.E., Heeney, M.M., Campagna, D.R., Aydinok, Y., Pearson, H.A., Hartman, K.R.,
1518 Mayo, M.M., Samuel, S.M., Strouse, J.J., Markianos, K., et al. (2008). Mutations in TMPRSS6
1519 cause iron-refractory iron deficiency anemia (IRIDA). Nat Genet *40*, 569–571.
1520 https://doi.org/10.1038/ng.130.

1521 54. Folgueras, A.R., de Lara, F.M., Pendás, A.M., Garabaya, C., Rodríguez, F., Astudillo, A.,
1522 Bernal, T., Cabanillas, R., López-Otín, C., and Velasco, G. (2008). Membrane-bound serine
1523 protease matriptase-2 (Tmprss6) is an essential regulator of iron homeostasis. Blood *112*,
1524 2539–2545. https://doi.org/10.1182/blood-2008-04-149773.

1525 55. Silvestri, L., Pagani, A., Nai, A., De Domenico, I., Kaplan, J., and Camaschella, C. (2008). The
1526 serine protease matriptase-2 (TMPRSS6) inhibits hepcidin activation by cleaving membrane
1527 hemojuvelin. Cell Metab *8*, 502–511. https://doi.org/10.1016/j.cmet.2008.09.012.

1528 56. Nai, A., Pagani, A., Mandelli, G., Lidonnici, M.R., Silvestri, L., Ferrari, G., and Camaschella,
1529 C. (2012). Deletion of TMPRSS6 attenuates the phenotype in a mouse model of β-thalassemia.
1530 Blood *119*, 5021–5029. https://doi.org/10.1182/blood-2012-01-401885.

1531 57. Finberg, K.E., Whittlesey, R.L., Fleming, M.D., and Andrews, N.C. (2010). Down-regulation
1532 of Bmp/Smad signaling by Tmprss6 is required for maintenance of systemic iron homeostasis.
1533 Blood *115*, 3817–3826. https://doi.org/10.1182/blood-2009-05-224808.

1534 58. Manolova, V., Nyffenegger, N., Flace, A., Altermatt, P., Varol, A., Doucerain, C., Sundstrom,
1535 H., and Dürrenberger, F. (2019). Oral ferroportin inhibitor ameliorates ineffective
1536 erythropoiesis in a model of β-thalassemia. Journal of Clinical Investigation *130*, 491–506.
1537 https://doi.org/10.1172/JCI129382.

1538 59. Zumerle, S., Calì, B., Munari, F., Angioni, R., Di Virgilio, F., Molon, B., and Viola, A. (2019).
1539 Intercellular Calcium Signaling Induced by ATP Potentiates Macrophage Phagocytosis. Cell
1540 Rep *27*, 1-10.e4. https://doi.org/10.1016/j.celrep.2019.03.011.

1541 60. Shen, J., Wilbon, A.S., Zhou, M., and Pan, Y. (2023). Mechanism of Ca2+ transport by
1542 ferroportin. Elife *12*, e82947. https://doi.org/10.7554/eLife.82947.

1543 61. Wang, Y.-T., Trzeciak, A.J., Rojas, W.S., Saavedra, P., Chen, Y.-T., Chirayil, R., Etchegaray,
1544 J.I., Lucas, C.D., Puleston, D.J., Keshari, K.R., et al. (2023). Metabolic adaptation supports
1545 enhanced macrophage efferocytosis in limited-oxygen environments. Cell Metab *35*, 316-
1546 331.e6. https://doi.org/10.1016/j.cmet.2022.12.005.

1547 62. Bhutia, Y.D., and Ganapathy, V. (2016). Glutamine transporters in mammalian cells and their
1548 functions in physiology and cancer. Biochimica et Biophysica Acta (BBA) - Molecular Cell
1549 Research *1863*, 2531–2539. https://doi.org/10.1016/j.bbamcr.2015.12.017.

1550 63. Beard, J. (2003). Iron deficiency alters brain development and functioning. J Nutr *133*, 1468S-
1551 72S. https://doi.org/10.1093/jn/133.5.1468S.

1552 64. Badaracco, M.E., Ortiz, E.H., Soto, E.F., Connor, J., and Pasquini, J.M. (2008). Effect of
1553 transferrin on hypomyelination induced by iron deficiency. J Neurosci Res *86*, 2663–2673.
1554 https://doi.org/10.1002/jnr.21709.

1555 65. Jiang, Y., Li, C., Wu, Q., An, P., Huang, L., Wang, J., Chen, C., Chen, X., Zhang, F., Ma, L., et
1556 al. (2019). Iron-dependent histone 3 lysine 9 demethylation controls B cell proliferation and
1557 humoral immune responses. Nat Commun *10*, 2935. https://doi.org/10.1038/s41467-019-
1558 11002-5.

1559 66. Zhu, L., Li, G., Liang, Z., Qi, T., Deng, K., Yu, J., Peng, Y., Zheng, J., Song, Y., and Chang, X.
1560 (2023). Microbiota-assisted iron uptake promotes immune tolerance in the intestine. Nat
1561 Commun *14*, 2790. https://doi.org/10.1038/s41467-023-38444-2.

1562 67. Frost, J.N., Wideman, S.K., Preston, A.E., Teh, M.R., Ai, Z., Wang, L., Cross, A., White, N.,
1563 Yazicioglu, Y., Bonadonna, M., et al. (2022). Plasma iron controls neutrophil production and
1564 function. Sci Adv *8*, eabq5384. https://doi.org/10.1126/sciadv.abq5384.

1565 68. Frost, J.N., Tan, T.K., Abbas, M., Wideman, S.K., Bonadonna, M., Stoffel, N.U., Wray, K.,
1566 Kronsteiner, B., Smits, G., Campagna, D.R., et al. (2021). Hepcidin-Mediated Hypoferremia
1567 Disrupts Immune Responses to Vaccination and Infection. Med *2*, 164-179.e12.
1568 https://doi.org/10.1016/j.medj.2020.10.004.

1569 69. Wang, L., Johnson, E.E., Shi, H.N., Allan Walker, W., Wessling-Resnick, M., and Cherayil,
1570 B.J. (2008). Attenuated inflammatory responses in hemochromatosis reveal a role for iron in
1571 the regulation of macrophage cytokine translation. J Immunol *181*, 2723–2731.

1572 70. Agoro, R., Taleb, M., Quesniaux, V.F.J., and Mura, C. (2018). Cell iron status influences
1573 macrophage polarization. PLoS One *13*, e0196921.
1574 https://doi.org/10.1371/journal.pone.0196921.

1575 71. Xu, W., Barrientos, T., Mao, L., Rockman, H.A., Sauve, A.A., and Andrews, N.C. (2015).
1576 Lethal Cardiomyopathy in Mice Lacking Transferrin Receptor in the Heart. Cell Rep *13*, 533–
1577 545. https://doi.org/10.1016/j.celrep.2015.09.023.

1578 72. Papathanassiu, A.E., Ko, J.-H., Imprialou, M., Bagnati, M., Srivastava, P.K., Vu, H.A., Cucchi,
1579 D., McAdoo, S.P., Ananieva, E.A., Mauro, C., et al. (2017). BCAT1 controls metabolic
1580 reprogramming in activated human macrophages and is associated with inflammatory diseases.
1581 Nat Commun *8*, 16040. https://doi.org/10.1038/ncomms16040.

1582 73. Lu, M., Luo, D., Zhang, Z., Ouyang, F., Shi, Y., Hu, C., Su, H., Li, Y., Zhang, J., Gui, Q., et al.
1583 (2024). Branched-chain amino acid catabolism promotes M2 macrophage polarization. Front.
1584 Immunol. *15*, 1469163. https://doi.org/10.3389/fimmu.2024.1469163.

1585 74. Yan, H., Liu, Y., Li, X., Yu, B., He, J., Mao, X., Yu, J., Huang, Z., Luo, Y., Luo, J., et al. (2024).
1586 Leucine alleviates cytokine storm syndrome by regulating macrophage polarization via the
1587 mTORC1/LXRα signaling pathway. eLife *12*, RP89750. https://doi.org/10.7554/eLife.89750.

75. Banerjee, S., Lu, S., Jain, A., Wang, I., Tao, H., Srinivasan, S., Nemeth, E., and He, P. (2024). Targeting PKCa alleviates iron overload in diabetes and hemochromatosis through the inhibition of ferroportin. Blood, blood.2024023829. https://doi.org/10.1182/blood.2024023829.

76. Ennerfelt, H., Frost, E.L., Shapiro, D.A., Holliday, C., Zengeler, K.E., Voithofer, G., Bolte, A.C., Lammert, C.R., Kulas, J.A., Ulland, T.K., et al. (2022). SYK coordinates neuroprotective microglial responses in neurodegenerative disease. Cell *185*, 4135-4152.e22. https://doi.org/10.1016/j.cell.2022.09.030.

77. Wang, S., Sudan, R., Peng, V., Zhou, Y., Du, S., Yuede, C.M., Lei, T., Hou, J., Cai, Z., Cella, M., et al. (2022). TREM2 drives microglia response to amyloid-β via SYK-dependent and -independent pathways. Cell *185*, 4153-4169.e19. https://doi.org/10.1016/j.cell.2022.09.033.

78. Kobayashi, A., Azuma, K., Takeiwa, T., Kitami, T., Horie, K., Ikeda, K., and Inoue, S. (2023). A FRET-based respirasome assembly screen identifies spleen tyrosine kinase as a target to improve muscle mitochondrial respiration and exercise performance in mice. Nat Commun *14*, 312. https://doi.org/10.1038/s41467-023-35865-x.

79. Canton, J., Khezri, R., Glogauer, M., and Grinstein, S. (2014). Contrasting phagosome pH regulation and maturation in human M1 and M2 macrophages. Mol Biol Cell *25*, 3330–3341. https://doi.org/10.1091/mbc.E14-05-0967.

80. Das Gupta, K., Shakespear, M.R., Curson, J.E.B., Murthy, A.M.V., Iyer, A., Hodson, M.P., Ramnath, D., Tillu, V.A., von Pein, J.B., Reid, R.C., et al. (2020). Class IIa Histone Deacetylases Drive Toll-like Receptor-Inducible Glycolysis and Macrophage Inflammatory Responses via Pyruvate Kinase M2. Cell Rep *30*, 2712-2728.e8. https://doi.org/10.1016/j.celrep.2020.02.007.

81. Codo, A.C., Davanzo, G.G., Monteiro, L. de B., de Souza, G.F., Muraro, S.P., Virgilio-da-Silva, J.V., Prodonoff, J.S., Carregari, V.C., de Biagi Junior, C.A.O., Crunfli, F., et al. (2020). Elevated Glucose Levels Favor SARS-CoV-2 Infection and Monocyte Response through a HIF-1α/Glycolysis-Dependent Axis. Cell Metab *32*, 437-446.e5. https://doi.org/10.1016/j.cmet.2020.07.007.

82. Van den Bossche, J., O'Neill, L.A., and Menon, D. (2017). Macrophage Immunometabolism: Where Are We (Going)? Trends Immunol *38*, 395–406. https://doi.org/10.1016/j.it.2017.03.001.

83. Divakaruni, A.S., Hsieh, W.Y., Minarrieta, L., Duong, T.N., Kim, K.K.O., Desousa, B.R., Andreyev, A.Y., Bowman, C.E., Caradonna, K., Dranka, B.P., et al. (2018). Etomoxir Inhibits Macrophage Polarization by Disrupting CoA Homeostasis. Cell Metab *28*, 490-503.e7. https://doi.org/10.1016/j.cmet.2018.06.001.

84. Liu, P.-S., Wang, H., Li, X., Chao, T., Teav, T., Christen, S., Di Conza, G., Cheng, W.-C., Chou, C.-H., Vavakova, M., et al. (2017). α-ketoglutarate orchestrates macrophage activation through metabolic and epigenetic reprogramming. Nat Immunol *18*, 985–994. https://doi.org/10.1038/ni.3796.

1627 85. Mills, E.L., Kelly, B., Logan, A., Costa, A.S.H., Varma, M., Bryant, C.E., Tourlomousis, P.,
1628 Däbritz, J.H.M., Gottlieb, E., Latorre, I., et al. (2016). Succinate Dehydrogenase Supports
1629 Metabolic Repurposing of Mitochondria to Drive Inflammatory Macrophages. Cell *167*, 457-
1630 470.e13. https://doi.org/10.1016/j.cell.2016.08.064.

1631 86. Chia, X.X., Ozols, E., Nikolic-Paterson, D.J., and Tesch, G.H. (2025). Spleen tyrosine kinase
1632 signaling in myeloid cells promotes macrophage infiltration, glomerulosclerosis, and
1633 interstitial fibrosis in diabetic kidney disease. Am J Physiol Renal Physiol *329*, F872–F882.
1634 https://doi.org/10.1152/ajprenal.00289.2025.

1635 87. Chen, L., Zhu, F., Gao, X., Yang, Y., Jin, G., Zhou, Y., Dong, G., and Zhou, G. (2025). Spleen
1636 tyrosine kinase aggravates intestinal inflammation through regulating inflammatory responses
1637 of macrophage in ulcerative colitis. Int Immunopharmacol *148*, 114122.
1638 https://doi.org/10.1016/j.intimp.2025.114122.

1639 88. Rohila, D., Park, I.H., Pham, T.V., Weitz, J., Hurtado de Mendoza, T., Madheswaran, S., Ishfaq,
1640 M., Beaman, C., Tapia, E., Sun, S., et al. (2023). Syk Inhibition Reprograms Tumor-Associated
1641 Macrophages and Overcomes Gemcitabine-Induced Immunosuppression in Pancreatic Ductal
1642 Adenocarcinoma. Cancer Res *83*, 2675–2689. https://doi.org/10.1158/0008-5472.CAN-22-
1643 3645.

1644 89. Torrance, J.D., and Bothwell, T.H. (1968). A simple technique for measuring storage iron
1645 concentrations in formalinised liver samples. S Afr J Med Sci *33*, 9–11.

1646 90. Picelli, S., Björklund, Å.K., Faridani, O.R., Sagasser, S., Winberg, G., and Sandberg, R. (2013).
1647 Smart-seq2 for sensitive full-length transcriptome profiling in single cells. Nat Methods *10*,
1648 1096–1098. https://doi.org/10.1038/nmeth.2639.

1649 91. Moggridge, S., Sorensen, P.H., Morin, G.B., and Hughes, C.S. (2018). Extending the
1650 Compatibility of the SP3 Paramagnetic Bead Processing Approach for Proteomics. J Proteome
1651 Res *17*, 1730–1740. https://doi.org/10.1021/acs.jproteome.7b00913.

1652 92. Hughes, C.S., Foehr, S., Garfield, D.A., Furlong, E.E., Steinmetz, L.M., and Krijgsveld, J.
1653 (2014). Ultrasensitive proteome analysis using paramagnetic bead technology. Mol Syst Biol
1654 *10*, 757. https://doi.org/10.15252/msb.20145625.

1655 93. Werner, T., Sweetman, G., Savitski, M.F., Mathieson, T., Bantscheff, M., and Savitski, M.M.
1656 (2014). Ion coalescence of neutron encoded TMT 10-plex reporter ions. Anal Chem *86*, 3594–
1657 3601. https://doi.org/10.1021/ac500140s.

1658 94. Yang, F., Shen, Y., Camp, D.G., and Smith, R.D. (2012). High-pH reversed-phase
1659 chromatography with fraction concatenation for 2D proteomic analysis. Expert Rev Proteomics
1660 *9*, 129–134. https://doi.org/10.1586/epr.12.15.

1661